Research Article

Amar Bestani, Choukri Lekbir*, and Abdelbaki Benmounah

Impact of calcination temperature, organic additive percentages, and testing temperature on the rheological behaviour of dried sewage sludge

https://doi.org/10.1515/arh-2024-0025
received July 31, 2024; accepted November 08, 2024

Abstract: The main objective of the present work is to evaluate the influence of calcination pretreatment (600–1,000°C), organic additive incorporation (4% methocel, 4% amijel, and 8% starch), and testing temperature (20–60°C) on the rheological flow behaviour of dried sewage sludge and sewage sludge ashes. Besides, the dependency of sludge systems rheology on total solid content (4–15%) and methocel percentage (3–6%) was also evaluated. Furthermore, characterization techniques such as thermal gravimetric analysis-differential scanning calorimetry, X-ray fluorescence, X-ray diffraction, Brunauer–Emmett–Teller, and scanning electron microscopy were employed to investigate, respectively, the thermal decomposition, the chemical composition, the structural variations, the specific surface area, the surface morphology, and microstructure of sludges. The analysis of rheological characteristics according to best-fitting rheological models such as Herschel–Bulkley, Ostwald–de Waele, Cross, and Carreau models revealed that the yield stress (τ_0) and infinite apparent viscosity (η_∞) increase with an increase in TS or methocel percentage and decrease with increasing calcination or testing temperature. The strong impact of testing temperature concerning the reduction of the viscosity involves high activation energy (E_a). This last criterion was used to compare the inter-particle strength of sludge systems.

Keywords: sewage sludge ash, TGA-DSC, XRD, BET specific surface area, rheology

*** Corresponding author: Choukri Lekbir**, Department of Chemistry, Faculty of Science, University M'Hamed Bougara of Boumerdès, Boumerdès, Algeria; Research Unit of Materials: Processes and Environment (UR-MPE), University M'Hamed Bougara of Boumerdès, Boumerdès, Algeria, e-mail: choukri.lekbir@univ-boumerdes.dz
Amar Bestani, Abdelbaki Benmounah: Research Unit of Materials: Processes and Environment (UR-MPE), University M'Hamed Bougara of Boumerdès, Boumerdès, Algeria

1 Introduction

Sustainable sewage sludge treatment requires optimal efficient facilities and strategies, including transport, storage, reduce, reuse, recycle, or disposal of sewage sludge [1–11]. Ecological friendly solutions and best alternative techniques for the reuse and final disposal of sewage sludge, as well as dewatering, composting, anaerobic digestion, drying-incineration, pelletizing, and sanitary landfill, are currently the key factors that control and improve the quality and efficiency of sewage sludge management [12–15].

The main objectives of sludge management are, on the one hand, to ensure high safety of human health and the environment from the hazardous substances present in sludge biomass such as organic pollutants, microplastics, pathogenic organisms, heavy metals, metalloids, leachate or landfill gas, and flue gas emission caused by sludge incineration [16–20]. On the other hand, to exploit the opportunity of its beneficial cost-effective reuse for the development of different fields such as agriculture and city green plantation (as soil conditioner-fertilizer) [21–24], anaerobic bioenergy recovery (as a precursor for methane-rich biogas production and heat or electricity conversion) [21,22,25,26], construction building materials (as a raw material and an ash additive for the manufacturing of pavers, bricks, tiles, geopolymer in cement and concrete, ceramics, glass, self-compacting and flowable fillers for pipeline bedding and foundation backfill) [21,22,27–31], and depollution of industrial wastewater effluents (as a powder adsorbent for the removal of dyes and a paste for the manufacturing of flat or tubular microfiltration membrane) [32–35].

The successful disposal or reuse of sewage sludge, generated by the wastewater treatment plants (WWTPs), depends strongly on the evolutionary history of sludge characteristics, which takes into account the origin of sludge (domestic, urban, agricultural, or industrial), its types (raw primary sludge, excess or thickened excess

activated sludge [TEAS], mixed sludge, digested sludge, or biosolid), its moisture content and particle size distribution, its chemical composition (metal ions and silica, organic matter, nutrition, nitrogen [N], phosphorus [P], potassium [K], and heavy metals), its structure and microstructure (amorphous or crystalline phases and sludge morphology), and its rheological behaviour (viscosity and shearing behaviour) [36–49]. This last characteristic, defined as the study of flow and deformation behaviour of sludge submitted under mechanical stress fields, is considered a crucial vital factor for the handling of sludge, either outside or inside the municipal sewage sludge treatment plants (pumping, mixing, hydrodynamic, mass transfer rates, settling, and extrusion).

Generally, complex dilute sludge (1–2% solids) and concentrate sludge (3–10% solids) display a Newtonian liquid-like flow behaviour (constant apparent viscosity with yield stress) and a non-Newtonian solid-like flow behaviour (shear-thinning or thixotropic) [40,41,43–46,48]. The prediction of the correct rheological flow behaviour necessitates the implication of trust rheological models such as Bingham, Ostwald–de Waele (Power law), Herschel–Bulkley, Casson, Sisko, Carreau, and Cross in order to estimate the useful rheological parameters, notably yield stress, flow behaviour index, zero-shear rate apparent viscosity, infinite-shear rate apparent viscosity, and flow consistency coefficient [43,44,46,50,51]. These rheological parameters are highly affected by many factors including total solid content (TS), pH, shearing, temperature, dose of polymer or other species, sludge chemical composition, and organic content [42,46,52–59].

Although the rheological characteristics of WWTP sludge are well studied to avoid the destruction of pumps, stirrers, and membrane bioreactor (MBR) equipment [60], the rheological characteristics of the sludge intended for ceramic paste preparation in order to manufacture flat or tubular microfiltration membrane support still remains unclear [35,61–63]. Commonly, sludge ash is a silica- and alumina-rich product, and it is likely an appropriate candidate raw material for the preparation of low-cost porous ceramic membrane, compared to costly metal oxides such as silica, alumina, zirconia, and titania [63,64].

The elaboration of porous tubular membrane supports by paste extrusion requires the incorporation of appropriate organic additives and a specific aging period to favour powder dispersion and the tuning of paste rheological behaviour. Employing cost-effective additives and co-incorporating sewage sludge ash (SSA) with natural minerals and industrial wastes (such as kaolin, dolomite, diatomite, bauxite, mullite, talc, and coal fly ash) are a promising cost-reduction strategy reducing the firing temperature and improving the mechanical strength and permeability of tubular membranes [63,64].

It is within this context that this work fits, in which the main aim is to highlight the effect of calcination temperature and organic additives such as amijel, methocel, and starch on the rheological behaviour of dried sewage sludge (SS0). Particular attention is paid to the evolution of sludge rheological characteristics in relation to TS, organic additives percentage, and testing temperature variations. Hence, additional analyses such as thermal gravimetric analysis (TGA), differential scanning calorimetry (DSC), X-ray fluorescence spectrometry (XRF), X-ray diffraction (XRD), Brunauer–Emmett–Teller (BET), and scanning electron microscopy (SEM) were also solicited to characterize the SS0 and SSAs.

2 Materials and methods

2.1 Dried sewage sludge samples and organic additives

The sludge used in this study is a drying bed-activated sludge provided by the Oued D'Hous WWTP (Bouira, Algeria), operating with an average wastewater flow of 25,840 m^3/day. After receiving a large quantity of sludge, samples were first heated in a furnace at a heating rate of 2°C/min to 250°C and held at this temperature for 120 min. Then, the temperature was increased at a rate of 5°C/min to the final calcination temperature and held at different calcination temperatures (600, 700, 750, 800, 850, 900, 950, and 1,000°C) for 180 min. After calcination, both uncalcined and calcined sludges were crushed and sieved using a 100 µm mesh sieve to obtain fine powders.

The following organic additives were mixed with the sludge powders (uncalcined and calcined) in order to study their rheological behaviours: soluble starch (Biochem Chemopharma), which acts as a porosity agent and binder; methocel (90 HG, methyl cellulose) (The Dow Chemical Company), which is a cellulose derivative used as a plasticizer; and amijel (Cplus 12072, cerestar), which is a derivative product consisting of pre-gelled starch used as a binder (gelling agent).

2.2 Chemical composition analysis

The chemical composition of SS0 and SSAs obtained at different calcination temperatures (600, 700, 750, 800,

850, 900, and 950°C) was determined by XRF spectrometry using a sequential wavelength-dispersive spectrometer (Bruker-AXS: S8 TIGER) equipped with a rhodium anode. The concentration of an unknown sample was determined using the Spectra plus software. Calibration curves were plotted for each element after having fixed all measurement parameters (accelerating voltage [60 kV], emission current [170 mA], crystal analyser, collimator, emission wavelength, measurement time, and detector).

2.3 Loss on ignition (LOI) analysis

This analysis aims to follow the evolution of mass loss in sludge samples during their calcination. A sludge sample with an initial mass of 5 g was placed in a porcelain crucible that had been dried and weighed beforehand. The assembly was placed in a furnace set at one of the calcination temperatures (600, 700, 750, 800, 850, 900, and 950°C) for 3 h. After cooling, the crucible is weighed and the mass loss of the sample is determined by the difference between the initial mass and the final mass for each calcination temperature.

2.4 Thermal analysis of SS0

Thermal analysis of SS0 was performed using a differential thermal analysis, TGA, and DSC simultaneous analyser (SDT Q600, TA Instruments). A sludge sample of about 43.74 mg was placed in an alumina crucible and was heated in a static air environment from room temperature to 1,100°C with a temperature rise of 5°C/min. The DSC analysis is used to identify phase transition and chemical reactions occurring in the form of endothermic (dehydration, dehydroxylation, vitreous transition, melting, etc.) or exothermic (oxidation, crystallization, etc.) heat flows. TG analysis permits the evaluation of mass loss related to the phase changes as a function of temperature.

2.5 Structural characterization

The crystalline phase mineralogy of SS0 and SSAs produced at different calcination temperatures (600, 700, 750, 800, 850, 900, 950, and 1,000°C) was assessed by using an X-ray diffractometer (Bruker D2 PHASER) equipped with a monochromatized CuKα radiation (λ = 1.54 Å), generated at 20 mA and 40 kV. The data were collected in the range 2θ from 5° to 90° with the scan step of 0.02°. Then, X'Pert Highscore Plus software containing the JCPDS-ICDD database was used to index the peaks of the different phases detected in the experimental diffraction patterns.

2.6 Specific surface area and pore diameter characterization

Nitrogen adsorption–desorption isotherms of SS0 and SSA (SSA600, SSA700, SSA750, SSA800, SSA850, SSA900, and SSA950) samples were measured at liquid nitrogen temperature (77 K) using a Quantachrome Instruments v11.0 adsorption analyser. The achieved data were handled by NovaWin ©1994-2010 software. Then, the specific surface area was calculated by the multi-point BET method, and the average pore diameter was estimated from the pore volume based on the application of the Kelvin equation. It is suitable to classify pores according to their size (IUPAC classification, 1985 [65]): (1) pores with diameters below 2 nm are called micropores, (2) pores of diameters comprised between 2 and 50 nm are called mesopores, and (3) pores with diameters above 50 nm are called macropores.

2.7 Surface morphology and microstructure characterization

The microstructural morphology of SS0 and SSA (SSA600, SSA700, SSA750, SSA800, SSA850, SSA900, SSA950, and SSA1000) samples was observed at different magnification scales by SEM via an SEM FEI quanta 250 instrument equipped with a tungsten filament using an acceleration voltage of 10 kV, a working distance of 10 mm, and a spot size of 3.5 nm.

2.8 Rheological measurements

The rheological behaviour of SS0 and SSA (SSA800, SSA850, SSA900, and SSA950) was studied in the presence and absence of organic additives (starch, methocel, and amijel) at different testing temperatures (20, 30, 40, 50, and 60°C), using an advanced rotational rheometer (type AR 2000, TA-instruments), connected to cryostat-controlled circulating

water maintained the Peltier concentric conical cylinder system at a constant temperature. The concentric cylinder system is composed of a water jacket, an inner cylinder (a cup with a diameter of 30 mm), and an MV rotor (an aluminium DIN bob with a diameter of 28 mm and length of 42 mm). The operational gap between the bob and the cylindrical cup is 5.92 mm.

In each measurement (three repeated analyses), a 20 mL volume of SS0 or SSA samples (mixed with and without organic additives) prepared by distilled water at different TS concentrations (TS = 4, 7, 10, 13, and 15%) was placed in the cylindrical cup. The rotating bob was then immersed in the sample via a shaft. All rheological experiments were conducted in the following sequence:

1. Shear rate ramping step 1: measuring the shear stress (τ) and the apparent viscosity (η) by linearly increasing the shear rate ($\dot{\gamma}$) from 0 to 600 s^{-1} over 300 s,
2. Keeping the shear rate ($\dot{\gamma}$) at 600 s^{-1} for 5 s,
3. Shear rate ramping 2: measuring the shear stress (τ) and the apparent viscosity (η) by linear decreasing of the shear rate ($\dot{\gamma}$) from 600 to 0 s^{-1} over 300 s.

3 Results and discussion

3.1 Effect of calcination temperature on chemical composition and weight LOI

The chemical composition and LOI of SS0 and SSAs (SSA600, SSA700, SSA750, SSA800, SSA850, SSA900, and SSA950) are summarized in Table 1. It can be clearly seen that SS0 and SSAs are predominantly composed of alumina (Al_2O_3), lime (CaO), and silica (SiO_2), which brings good mechanical performance to these sludges. Considerable percentages of MgO, Fe_2O_3, SO_3, and P_2O_5, with a small amount of MnO, Na_2O, TiO_2, and K_2O oxides, were also detected. It can also be observed that the percentage content of oxide components and the weight LOI of the sludge ashes increased and decreased, respectively, as the calcination temperature increased. SSAs are mainly composed of SiO_2, Al_2O_3, Fe_2O_3, CaO, and P_2O_5 in the range (in wt%) of 30.70–32.89, 11.77–12.26, 5.52–6.03, 21.99–24.38, and 9.39–10.22, compared, respectively, to those ranged in 14.33–65.00, 2.65–34.20, 2.10–30.00, 1.10–40.10, and 0.30–26.70 given in the literature [31]. The weight LOI value ranges between 2.54 and 10.06 compared to those ranging in 1.40–41.80 reported in the literature [31]. The high value of LOI for SS0 (52.01 wt%) is due to its elevated organic matter content.

3.2 Thermal behaviour of SS0

TGA and DSC profiles of the SS0 are shown in Figure 1. The TGA curve shows that the weight loss increases with increasing temperature up to a total weight loss of 57.09 wt%. The thermal decomposition of sludge can occur through four kinetic stages.

Stage I (from room temperature to 100°C and from 100 to ~214°C), corresponding to the dehydration phenomenon, in which two weight losses were detected and attributed to water releases [66,67]. The first weight loss of 3.34 wt% detected at 100°C is attributed to the evaporation of free water physisorbed onto the sludge surface. This is accompanied by a small broad endothermic peak of DSC. The second one of 6.10 wt% detected at 214°C is associated with the departure of bound water inside the sludge.

Stage II (from 214 to 470°C), relating to the oxidation of organic matter, where two main weight losses of 18.18 and 19.55 wt% were observed and evidenced by the two exothermic peaks appear, respectively, at 347.09 and 441.34°C in the DSC curve.

Stage III (from 470 to 750°C), linking to the combustion of fixed carbon, proved by a weight loss of 6.31 wt% [67].

Stage IV (from 750 to 1,100°C), mainly owing to the decomposition of calcium carbonate ($CaCO_3$) into lime (calcium oxide, CaO) with a weight loss of 2.05 wt% (endothermic peak at ~768.50°C) [68], followed by the crystallization of the forsterite phase (exothermic peak at ~900°C) [69] (see the diffraction patterns in Figure 2), and finally the melting transition (endothermic peak at ~1057.60°C) with a weight loss of 1.14 wt%, most probably due to the decomposition of minerals such as siderite [70].

Based on the comparison between the DSC curve of SS0 and those reported by Majewsky et al. [71] and Rosario et al. [72] for pure plastic substances (polyethylene [PE], polyethylene terephthalate, high-density polyethylene, low-density polyethylene, polypropylene [PP], polyvinylchloride, polyamide, polyester, polyurethane, and polystyrene) and applied to measure PE and PP, it should be mentioned that no microplastics were detected in the SS0 sample. This reflects the higher microplastics removal efficiency of the WWTP process.

3.3 Effect of calcination temperature on crystalline structure of SS0

The XRD diffractograms of SS0 and SSA produced at different calcination temperatures (600, 700, 750, 800, 850, 900, 950, and 1,000°C) are depicted in Figure 2.

Table 1: Chemical composition and weight LOI of SS0 and SSAs

Compounds (wt%)	Dried sludge and sludge ashes							
	SS0	SSA600	SSA700	SSA750	SSA800	SSA850	SSA900	SSA950
Na_2O	0.250	0.380	0.360	0.390	0.380	0.420	0.400	0.410
MgO	1.640	2.910	2.960	3.020	3.010	3.030	3.050	3.080
Al_2O_3	6.420	11.770	12.080	12.160	12.170	12.180	12.200	12.260
SiO_2	15.520	30.700	33.120	32.550	32.580	32.830	33.140	32.890
P_2O_5	5.270	9.390	9.870	10.050	10.070	10.150	10.220	10.220
SO_3	3.300	4.730	4.680	4.770	5.000	5.140	5.150	5.170
K_2O	0.950	1.830	1.890	1.830	1.840	1.860	1.790	1.770
CaO	11.550	21.990	22.890	22.920	22.940	23.490	24.140	24.380
TiO_2	0.330	0.680	0.690	0.700	0.700	0.700	0.700	0.720
MnO	0.150	0.290	0.290	0.300	0.320	0.320	0.320	0.320
Fe_2O_3	2.580	5.520	5.660	5.680	5.700	5.920	6.020	6.030
Cr_2O_3	0.007	0.010	0.010	0.020	0.020	0.020	0.020	0.020
NiO	0.005	0.009	0.010	0.010	0.009	0.010	0.010	0.010
CuO	0.020	0.040	0.040	0.000	0.000	0.040	0.040	0.040
ZnO	0.060	0.140	0.150	0.150	0.160	0.160	0.170	0.170
SrO	0.020	0.040	0.050	0.050	0.060	0.070	0.070	0.070
Rb_2O	0.002	0.005	0.005	0.005	0.006	0.006	0.007	0.006
PbO	0.004	0.010	0.010	0.010	0.020	0.020	0.020	0.020
BaO	0.040	0.090	0.100	0.100	0.100	0.100	0.100	0.110
ZrO_2	0.002	0.005	0.006	0.006	0.008	0.009	0.010	0.010
Cl	0.100	0.100	0.120	0.110	0.100	0.090	0.060	0.050
LOI	52.010	10.060	5.020	5.560	5.760	3.880	3.110	2.540

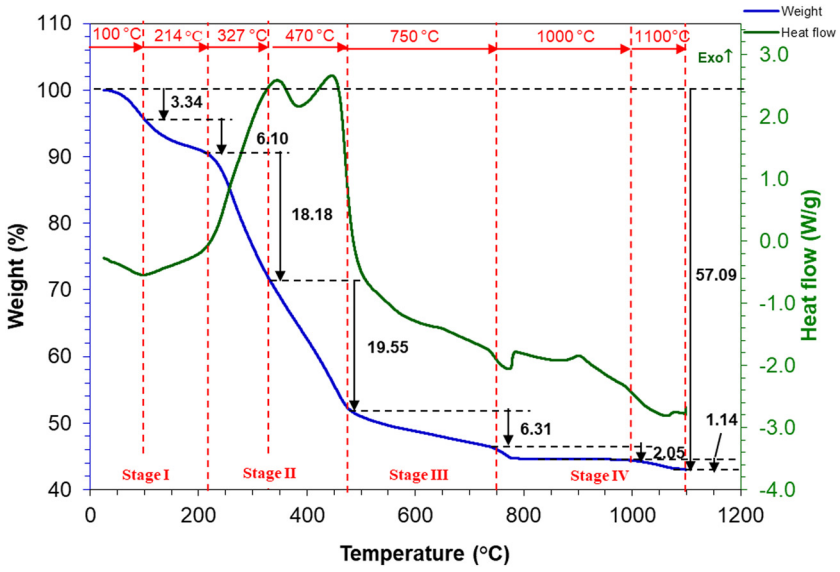

Figure 1: ATG-DSC of SS0.

The identification of different peaks present in the diffractogram of the SS0 revealed the existence of the following mineralogical phases: quartz (SiO_2), calcite ($CaCO_3$), illite ($K(Al_4Si_2O_9(OH)_3$), and magnetite (Fe_3O_4), with a small amount of kaolinite ($Al_4Si_4O_{10}(OH)_8$) and dolomite ($CaMg(CO_3)_2$). It can be noticed that in this case, the quartz and calcite are the major mineral phases.

The main mineral phases detected in the SSA prepared at 600°C are quartz (SiO_2), calcite ($CaCO_3$), illite ($K(Al_4Si_2O_9(OH)_3$), anhydrite ($CaSO_4$), albite ($NaAlSi_3O_8$)

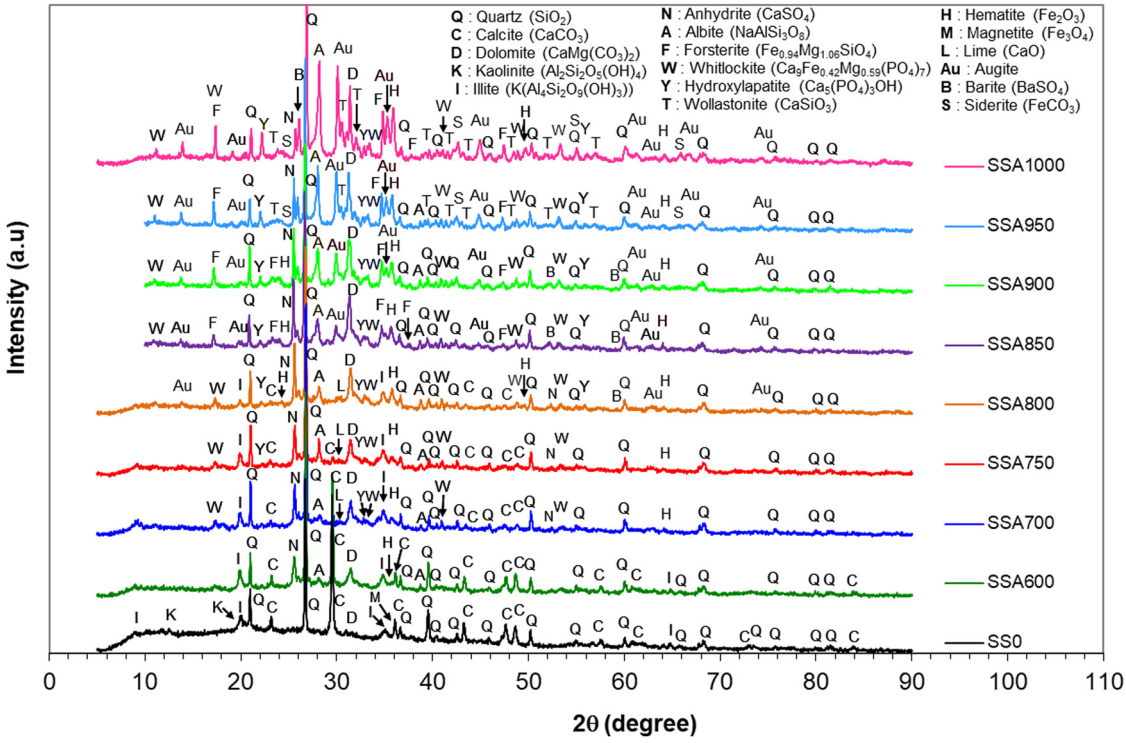

Figure 2: XRD diffractograms of SS0 and SSAs (SSA600, SSA700, SSA750, SSA800, SSA850, SSA900, SSA950, and SSA1000).

(feldspars), dolomite ($CaMg(CO_3)_2$), and small quantities of hematite as the first sign of appearance.

After calcination of sewage sludge at 700, 750, and 800°C, calcite decomposes ($CaCO_3$) into lime (calcium oxide, CaO) [68], accompanied in parallel by the formation of barite ($BaSO_4$), augite ($Na_{0.36}Ca_{2.46}Mg_{3.61}Fe_{0.84}Al_{1.37}Ti_{0.08}Si_{7.28}O_{24.00}$), whitlockite ($Ca_9Fe_{0.42}Mg_{0.59}(PO_4)_7$), and hydroxylapatite ($Ca_5(PO_4)_3OH$) [73]. The X-ray diffractograms of sewage sludge calcined at 850 and 900°C clearly illustrate the emergence of forsterite ($Fe_{0.94}Mg_{1.06}SiO_4$) phase at around 850°C with the entire disappearance of calcite that further indicates the achievement of thermal decomposition (Figure 1).

The mineralogical analysis of calcined sludge, at the high temperatures of 950 and 1,000°C, discloses the growth of siderite ($FeCO_3$) and wollastonite ($CaSiO_3$) phases [74,75].

3.4 Effect of calcination temperature on specific surface area and average pore diameter of SS0

The nitrogen adsorption–desorption isotherms (V_{N2} versus the reduced pressure $P_r = P/P_0$) and BET specific surface area with their corresponding average pore diameter of SS0 and SSA (SSA600, SSA700, SSA750, SSA800, SSA850, SSA900, and SSA950) samples are shown, respectively, in Figure 3a and b. It is clear from Figure 3a that all sludge samples (SS0 and SSA) show isotherms of type IV with an H3 hysteresis loop shape identified in the original IUPAC classification related to mesoporous materials [65]. Loops of this type are specified by non-rigid aggregates of plate-like particles (e.g., zeolites, clays, and also some activated carbons) or assemblages of slit-shaped pores [76].

It can first be seen in Figure 3b that the BET specific surface area decreases with increasing calcination temperature. The BET specific surface area of SSA is found to be in the range of 3.15–25.40 m^2/g compared to those ranging from 2.50 to 23.10 m^2/g available in the literature [31]. However, we can also observe in Figure 3b that the average pore diameter increases in the first stage from 5.96 nm (corresponding to SS0) to reach a maximum value of 26.58 nm (corresponding to SSA800), then it decreases in the second stage to reach a value of 9.6 nm (corresponding to SSA950). Therefore, it was confirmed that all pore diameters are included between 2 and 50 nm, indicating that the sludges (SS0 and SSA) are mesoporous adsorbents. The highest value of the average pore diameter (26.58 nm) is attributed to the creation of some new mesopores resulting, respectively, from the devolatilization of fixed carbon [67] and to some structural changes in SSA as calcite ($CaCO_3$) decomposition into lime (CaO) and formation of barite ($BaSO_4$) [68].

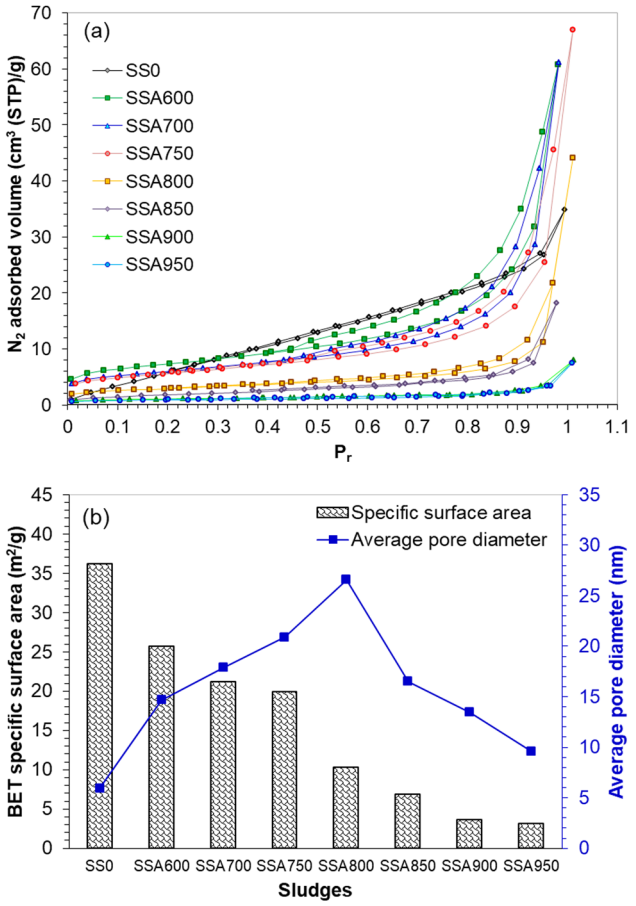

Figure 3: (a) Nitrogen adsorption–desorption isotherms and (b) BET specific surface area and average pore diameter of SS0 and SSAs (SSA600, SSA700, SSA750, SSA800, SSA850, SSA900, and SSA950).

3.5 Effect of calcination temperature on surface morphology and microstructure of SS0

The morphological micrographs of SS0 and SSAs (SSA600, SSA700, SSA750, SSA800, SSA850, SSA900, SSA950, and SSA1000) are exposed at two magnifications (×6,000 and ×12,000) in Figure 4. As seen from this figure, the heterogeneous surface of SS0 is smoother and less porous than SSA surfaces. It was mostly because the organic matter formed a smooth, dense microstructure, and the inorganic particles like quartz or calcite with spherical shape agglomerated and induced a rough surface morphology. The SSAs of finer grains are made of different-sized and irregular-shaped particles with porous and rough surface microstructure.

The pore formation could be attributed to the removal of ash and volatile organic matter during the calcination process [28]. It is clearly shown from SSA micrographs that when the calcination temperature increases from 600 to 800°C, the SSA microstructure becomes more and more porous and rough, with a larger pore diameter for SSA800. Beyond 800°C, the microstructure of SSA becomes less porous and less rough than the SSA800 microstructure, which is due not only to the appearance of larger SSA particles essentially agglomerated from many finer grains [31], but also to the development of crystalline phases at high calcination temperatures (Figure 2). These microstructural observations confirm the result obtained from pore diameter measurements (Figure 3b).

3.6 Rheological characterization

3.6.1 Rheological modelling of sludge flow

In the case of our sludge samples, several non-Newtonian rheological models, such as Bingham, Ostwald–de Waele (Power law), Herschel–Bulkley, Sisko, Carreau, and Cross models, were applied in order to fit the shear stress (τ) −shear rate ($\dot{\gamma}$) and apparent viscosity (η)−shear rate ($\dot{\gamma}$) curves. These rheological models used to simulate and estimate the rheological parameters, like yield stress, flow behaviour index, zero-shear rate apparent viscosity, infinite-shear rate apparent viscosity, and flow consistency coefficient, are defined in the following equations [43,44,46,50,51]:

Ostwald–de Waele model

$$\tau = K\dot{\gamma}^n. \tag{1}$$

(Shear-thinning, pseudoplastic: $K > 0$, $0 < n < 1$)
(Shear-thickening, dilatant: $K > 0$, $n > 1$)

Bingham model

$$\tau = \tau_0 + \eta_p\dot{\gamma}. \tag{2}$$

(Plastic: $K > 0$, $\tau_0 > 0$, $n = 1$)

Herschel–Bulkley model

$$\tau = \tau_0 + K\dot{\gamma}^n. \tag{3}$$

(Shear thickening, yield dilatant: $K > 0$, $\tau_0 > 0$, $1 < n < \infty$)
(Shear thinning, yield pseudoplastic: $K > 0$, $\tau_0 > 0$, $0 < n < \infty$)

Sisko model

$$\eta = \eta_\infty K\dot{\gamma}^{n-1}. \tag{4}$$

Carreau model

$$\eta = \eta_\infty + \left[(\eta_0 - \eta_\infty)(1 + (\lambda\dot{\gamma})^2)^{\frac{n-1}{2}}\right]. \tag{5}$$

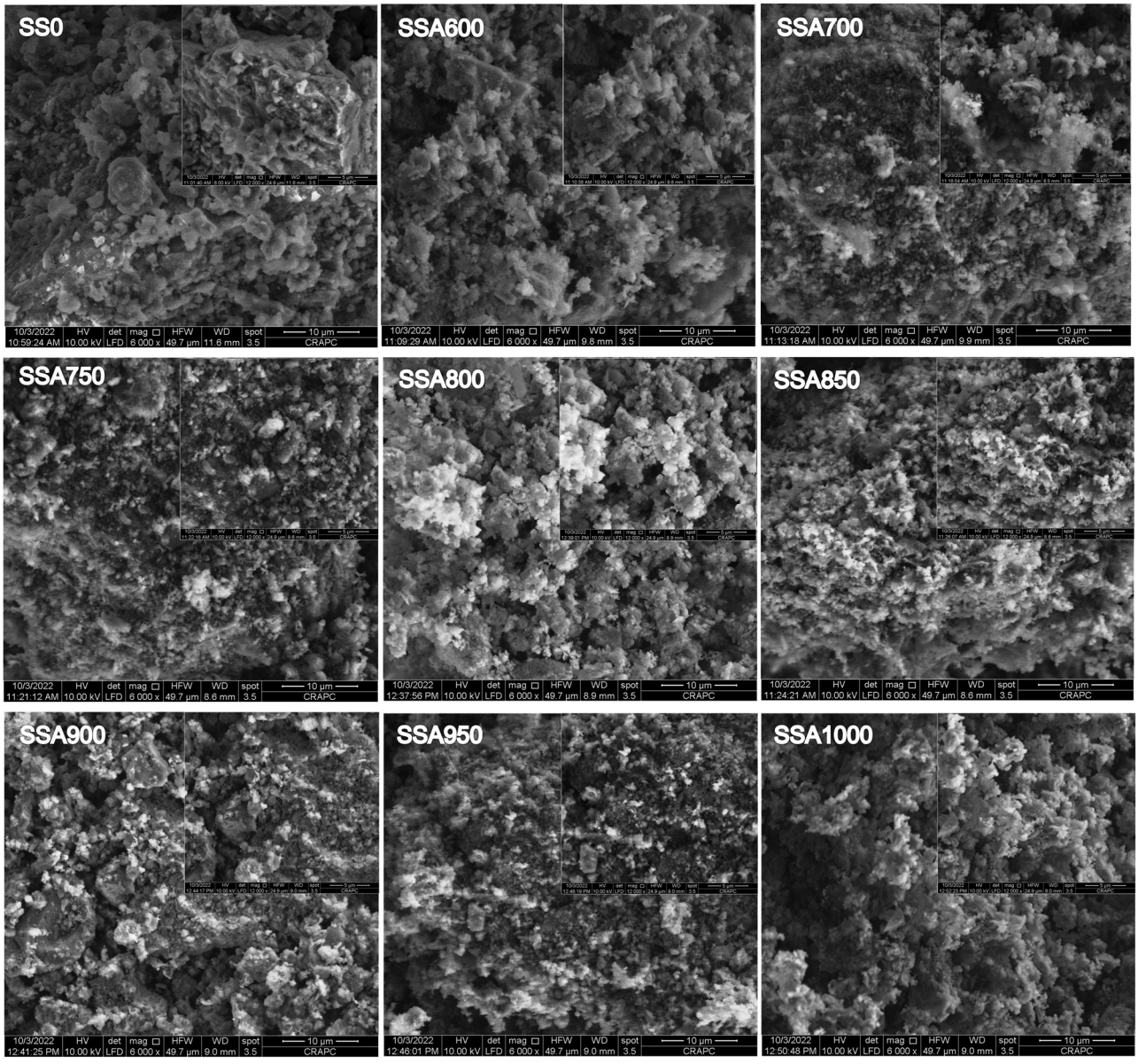

Figure 4: SEM images of SS0 and SSAs (SSA600, SSA700, SSA750, SSA800, SSA850, SSA900, SSA950, and SSA1000).

Cross model

$$\eta = \eta_\infty + \frac{(\eta_0 - \eta_\infty)}{1 + (\lambda\dot{\gamma})^m}, \tag{6}$$

where τ_0 is the yield stress (Pa), η_p is the plastic viscosity (Pa s), $\dot{\gamma}$ is the shear rate (s^{-1}), n is the flow behaviour index, K is the flow consistency coefficient (Pa s), η_∞ is the infinite-shear rate apparent viscosity (Pa s), η_0 is the zero-shear rate apparent viscosity (Pa s), λ is the time constant (s), and m is the Cross rate constant.

An example of an experimental rheological sequence (shear stress [τ]–shear rate [$\dot{\gamma}$] and apparent viscosity [η] –shear rate [$\dot{\gamma}$] curves) carried out on SS0 with TS = 4% is presented in Figure 5a and b (see Section 2.8).

3.6.2 Effect of TS and calcination temperature on the rheological behaviour of sewage sludge

The first step shear stress (τ)–shear rate ($\dot{\gamma}$) and apparent viscosity (η)–shear rate ($\dot{\gamma}$) curves of SS0 and SSAs, for different TS = 4, 7, 10, 13, and 15%, at 20°C, are plotted, respectively, with the best-fit rheological model in Figures 6 and 7.

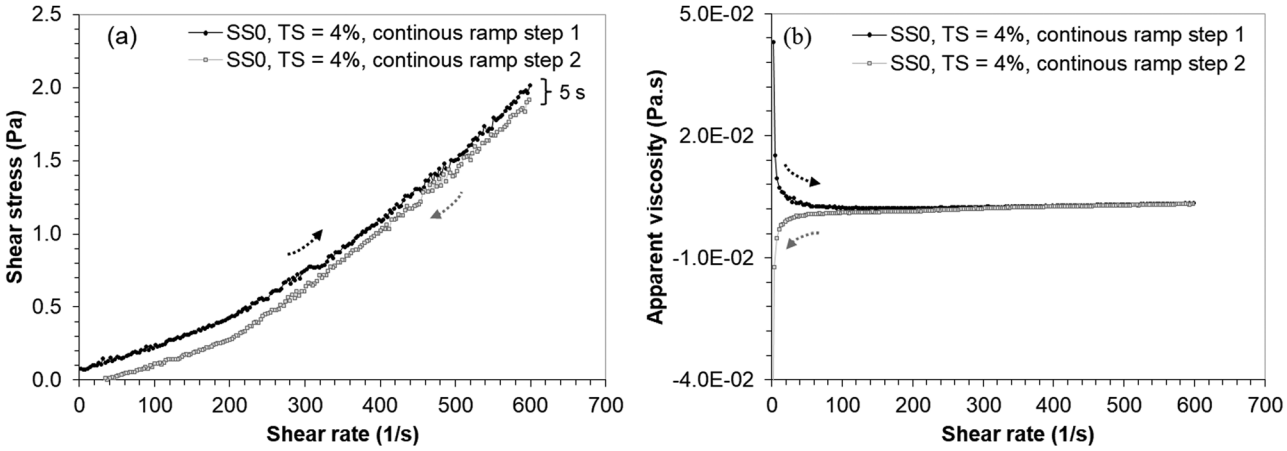

Figure 5: (a) Shear stress (τ)–shear rate ($\dot{\gamma}$) and (b) apparent viscosity (η)–shear rate ($\dot{\gamma}$) curves of SS0 for TS = 4%, at 20°C.

Figure 6 shows that for all sludge samples, the shear stress increases with increasing shear rate indicating non-Newtonian shear thickening (yield dilatant) flow behaviour. Such flow behaviour was also previously reported by a few authors [52,58]. From this figure, it could be realized that the thermal treatment of SS0 at different calcination temperatures has a decreasing impact on shear stress.

The shear stress (τ)–shear rate ($\dot{\gamma}$) experimental data were fitted to different rheological models discussed in equations (1)–(3). Several rheological parameters estimated from different models are given in Table 2, where the Herschel–Bulkley model was selected, referring to the high values of linear correlation coefficient (R^2), as the best model fitting the experimental data. According to the Herschel–Bulkley model, the increase in TS of all sludges resulted roughly in an increase of yield stress (τ_0). It can also be observed that an increase in TS from 4 to 13% caused a decrease in the flow consistency coefficient (K) and an increase in the flow behaviour index (n). However, at a higher value of TS (15%), these two rheological parameters (K and n) were significantly increased and decreased, respectively.

Figure 7 displays that, in the first regime, the apparent viscosity of all sludge samples decreases with an increase in shear rate until a critical shear rate ($\eta_C = \eta_\infty$), exhibiting a shear-thinning laminar behaviour. In the second regime, the apparent viscosity increases gradually with increasing shear rate to reach a maximum constant value (η_{max}), revealing a shear-thickening turbulent behaviour. Similar evolution behaviours have been reported by many researchers, such as Rosales et al. [77], Ratkovich et al. [43], Gienau et al. [57], and Edifor et al. [78], for other sludge systems.

From Figure 7, it could also be distinguished that the thermal treatment of SS0 at different calcination temperatures has a decreasing impact on the apparent viscosity. The apparent viscosity (η)–shear rate ($\dot{\gamma}$) experimental data of the first regime were fitted to different rheological models discussed in equations (4)–(6).

The various rheological parameters estimated from different models are given in Table 3, where the Cross model was selected, based on the high values of linear correlation coefficient (R^2), as the best model fitting the experimental data. According to the Cross model, the increase in sludge TS resulted in an increase of the infinite-shear rate apparent viscosity ($\eta_C = \eta_\infty$). This increase in viscosity is possibly due to the improvement of particle–particle interactions forming a network of particles during sludge addition [43,78]. Furthermore, for each sludge's TS, the increase in calcination temperature is accompanied by a decrease of the infinite-shear rate apparent viscosity ($\eta_C = \eta_\infty$). This is probably due, respectively, to the decrease of the weight LOI (organic matter content) (Table 1), the specific surface area, and the average pore diameter (Figure 3b) during the increase of the calcination temperature (800–950°C). A decrease in specific surface area and average pore diameter can result in the minimization of the water pathway, which in turn hinders the efficient interaction between sludge particles.

3.6.3 Effect of organic additive on the rheological behaviour of SSAs

The first step shear stress (τ)–shear rate ($\dot{\gamma}$) and apparent viscosity (η)–shear rate ($\dot{\gamma}$) curves of SSAs mixed with

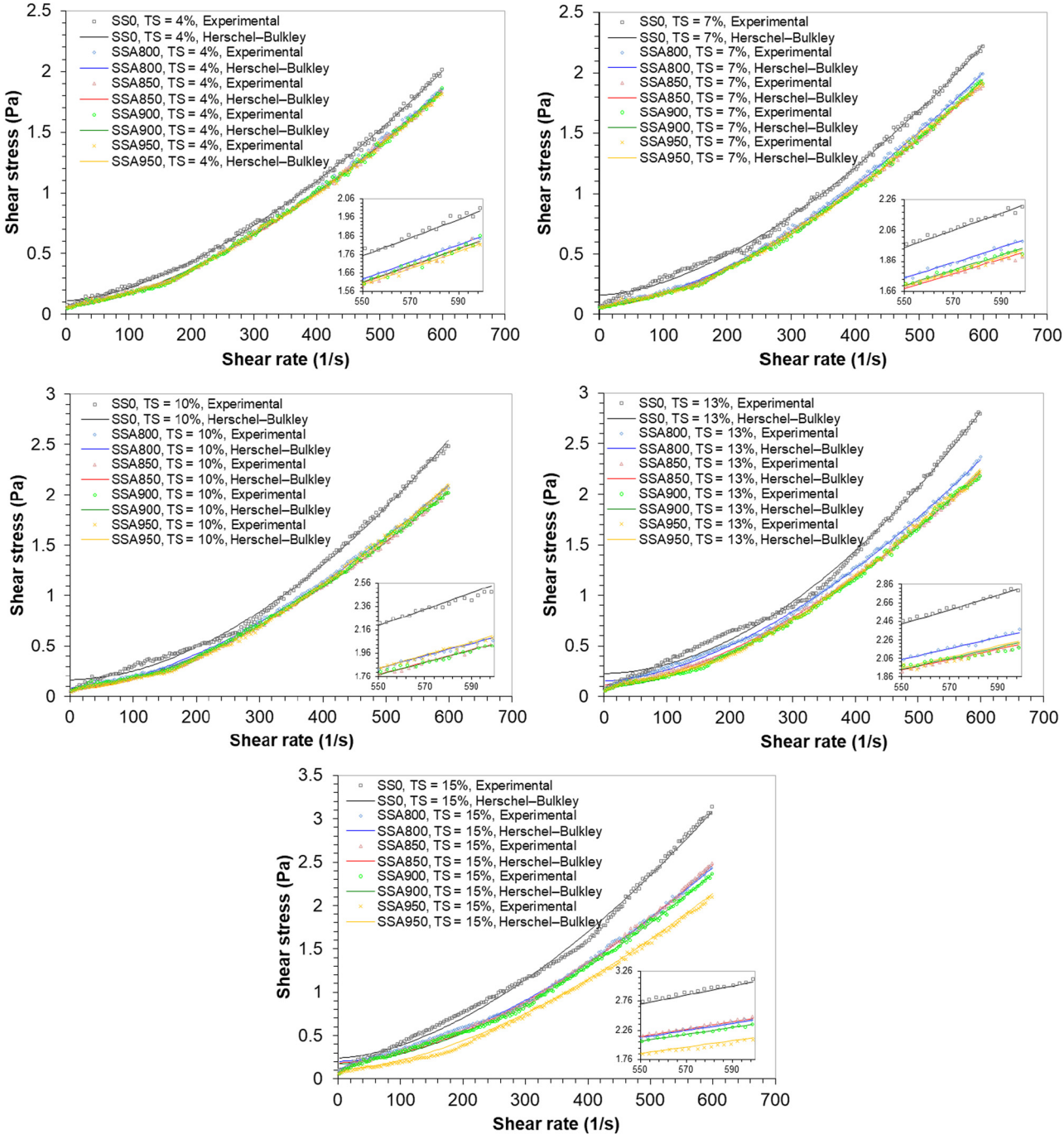

Figure 6: Shear stress (τ)–shear rate ($\dot{\gamma}$) curves of SS0 and SSAs for different TS = 4, 7, 10, 13, and 15%, at 20°C.

organic additives (proportion: 4% methocel + 4% amijel + 8% starch), for different TS = 4, 7, 10, 13, and 15%, at 20°C, are plotted, respectively, with the best-fit rheological model in Figures 8 and 9.

Figure 8 shows that for all SSA and organic additive mixtures, the shear stress increases with increasing shear rate indicating non-Newtonian shear thickening (yield dilatant) flow behaviour at low TS (4 and 7%) and shear-thinning (pseudoplastic) flow behaviour at high TS (10, 13, and 15%). As can be clearly seen in this figure, at TS = 4%, the shear stress increases with the increase of calcination temperature. Above TS = 4%, the shear stress decreases when the calcination temperature increases from 800 to 850°C, then it increases, respectively, to reach a maximum value when the calcination temperature increases from 900 to 950°C.

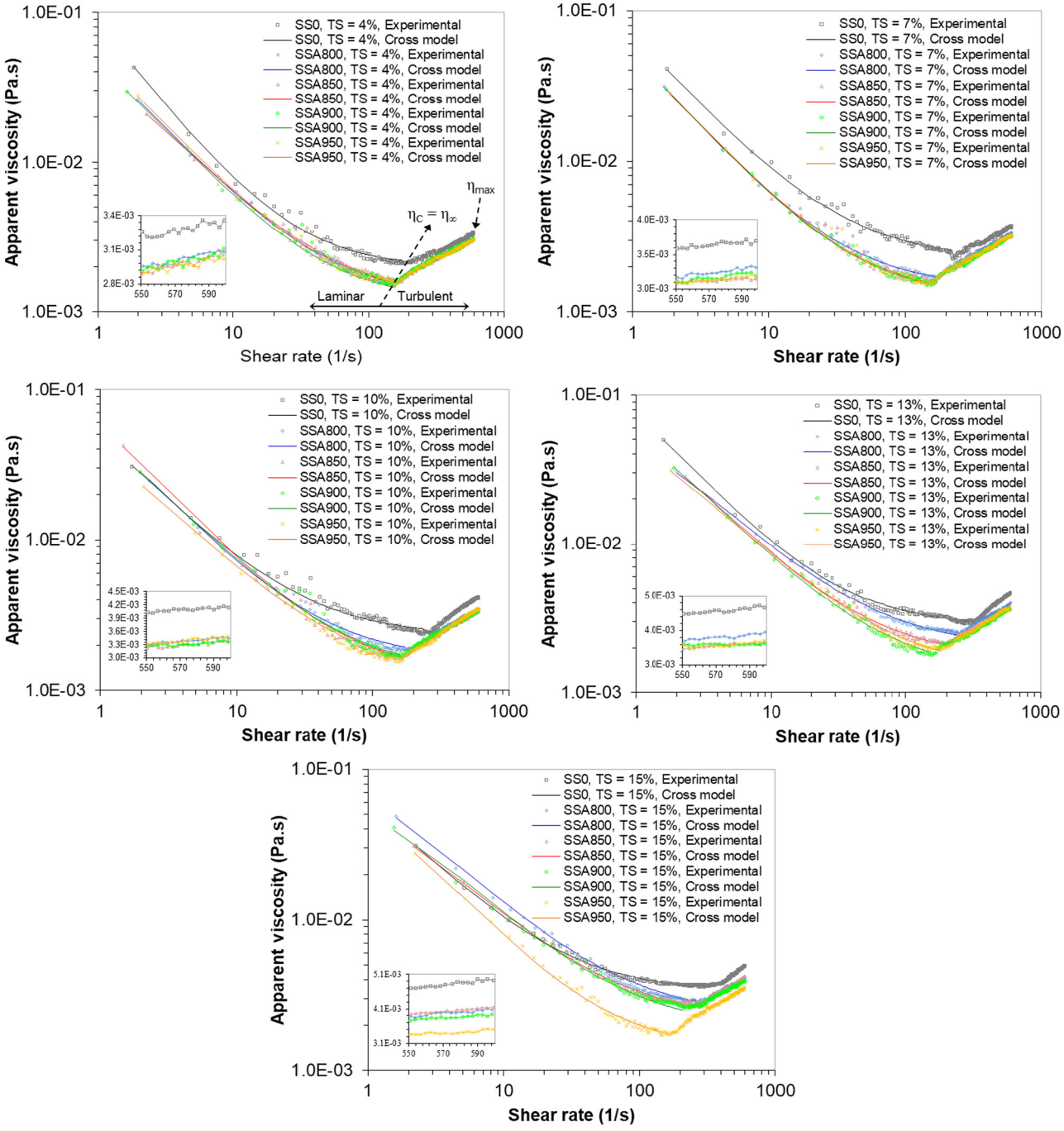

Figure 7: Apparent viscosity (η)–shear rate ($\dot{\gamma}$) curves of SS0 and SSAs, for different TS = 4, 7, 10, 13, and 15%, at 20°C.

The shear stress (τ)–shear rate ($\dot{\gamma}$) experimental data were fitted to different rheological models discussed in equations (1)–(3). The several rheological parameters estimated from different models are presented with a thixotropic area (reduced hysteresis area [rHa]) in Table 4, where the Herschel–Bulkley and Ostwald–de Waele models were privileged, referring to the high values of linear correlation coefficient (R^2) and the physical meaning, as the best models fitting the experimental data. The negative value of yield stress (τ_0), with no physical meaning, showing that the Herschel–Bulkley model was not suitable, and it was replaced in this situation by the Ostwald–de Waele model. Recently, two methods, namely, particle swarm optimization and genetic algorithm, were used as the best choice to obtain the most realistic solutions for both positive and negative yield stress values of different samples [79]. According to both models

Table 2: Fitting parameters of different shear stress rheological models for different TS of SS0 and SSAs at 20°C

Sludge	TS (%)	Herschel–Bulkley model				Ostwald–de Waele model		
		$\tau = \tau_0 + K\gamma^n$				$\tau = K\gamma^n$		
		τ_0 (Pa)	K (Pa s)	n	R^2	K (Pa s)	n	R^2
SS0	4	0.1123	6.43×10^{-5}	1.6082	0.9992	2.93×10^{-4}	1.3765	0.9944
	7	0.1584	5.20×10^{-5}	1.6558	0.9981	3.82×10^{-4}	1.3510	0.9900
	10	0.1628	2.15×10^{-5}	1.8161	0.9976	1.61×10^{-4}	1.5076	0.9900
	13	0.2282	1.62×10^{-5}	1.8736	0.9955	2.39×10^{-4}	1.4594	0.9834
	15	0.2413	7.17×10^{-5}	1.6555	0.9958	7.39×10^{-4}	1.2872	0.9854
SSA800	4	0.0640	6.65×10^{-5}	1.5952	0.9992	1.67×10^{-4}	1.4551	0.9973
	7	0.0699	5.73×10^{-5}	1.6302	0.9993	1.49×10^{-4}	1.4844	0.9973
	10	0.0846	5.81×10^{-5}	1.6344	0.9989	1.75×10^{-4}	1.4665	0.9962
	13	0.1545	4.82×10^{-5}	1.6764	0.9986	3.15×10^{-4}	1.3896	0.9915
	15	0.2013	5.36×10^{-5}	1.6634	0.9980	5.45×10^{-4}	1.3086	0.9872
SSA850	4	0.0670	6.46×10^{-5}	1.5974	0.9991	1.71×10^{-4}	1.4489	0.9970
	7	0.0645	5.99×10^{-5}	1.6169	0.9991	1.49×10^{-4}	1.4781	0.9973
	10	0.0698	5.63×10^{-5}	1.6359	0.9992	1.44×10^{-4}	1.4926	0.9972
	13	0.1135	5.37×10^{-5}	1.6532	0.9992	3.15×10^{-4}	1.4352	0.9948
	15	0.1855	4.47×10^{-5}	1.6948	0.9984	3.92×10^{-4}	1.3622	0.9890
SSA900	4	0.0615	7.46×10^{-5}	1.5755	0.9990	1.80×10^{-4}	1.4417	0.9973
	7	0.0665	4.77×10^{-5}	1.6548	0.9994	1.24×10^{-4}	1.5092	0.9975
	10	0.0768	5.10×10^{-5}	1.6507	0.9990	1.58×10^{-4}	1.4788	0.9967
	13	0.0941	4.03×10^{-5}	1.7012	0.9992	1.36×10^{-4}	1.5153	0.9960
	15	0.1729	5.53×10^{-5}	1.6554	0.9983	4.25×10^{-4}	1.3438	0.9898
SSA950	4	0.0640	6.91×10^{-5}	1.5860	0.9992	4.84×10^{-3}	1.4441	0.9973
	7	0.0629	5.34×10^{-5}	1.6364	0.9992	1.30×10^{-4}	1.5001	0.9975
	10	0.0657	3.98×10^{-5}	1.6962	0.9991	9.70×10^{-5}	1.5599	0.9974
	13	0.1012	3.90×10^{-5}	1.7070	0.9988	1.43×10^{-4}	1.5086	0.9952
	15	0.1097	5.22×10^{-5}	1.6521	0.9991	1.49×10^{-4}	1.4919	0.9967

(Herschel–Bulkley and Ostwald–de Waele), the increase in TS of SSA and organic additives mixtures resulted roughly in an increase of yield stress (τ_0), a decrease in flow behaviour index (n) and an increase in flow consistency coefficient (K).

It can also be seen that an increase in TS from 4 to 13% led to an increase in rHa. However, at a higher value of TS (15%), no thixotropic (NT) behaviour was detected. This non-thixotropy detected at TS = 15% may be due to a competition between solid interactions and viscous forces, and it seems quite logical that the stronger the viscous forces, the lower the degree of thixotropy [41].

Moreover, as can be remarked from Table 4, according to the TS, the calcination temperature significantly influences the thixotropic area (rHa). For TS = 4%, the rHa increases from 18.87 to 58.18 Pa s^{-1} when the calcination temperature increases from 800 to 900°C, then it decreases to a value of 56.79 Pa s^{-1} for a calcination temperature of 950°C. For TS = 7%, the rHa decreases from 82.19 to 58.35 Pa s^{-1} when the calcination temperature increases from 800 to 950°C. For TS = 10%, the rHa decreases from 242.35 to 175.48 Pa s^{-1} when the calcination temperature increases from 800 to 850°C, then it increases to 268.27 Pa s^{-1} at 900°C; after that, it decreases to a value of 219.88 Pa s^{-1} for a calcination temperature of 950°C. For TS = 13%, the rHa decreases from 525.66 to 233.02 Pa s^{-1} when the calcination temperature increases from 800 to 900°C.

Figure 9 shows that, according to the TS, mixtures of SSA and organic additives exhibit different viscosity behaviours, where in general the apparent viscosity decreases with increasing shear rates, revealing a shear-thinning behaviour. From this figure, it could be remarked that for TS = 4%, the apparent viscosity increases with the increase of calcination temperature. Above TS = 4%, the apparent viscosity decreases when the calcination temperature increases from 800 to 850°C, then it increases respectively with a big range to reach a maximum value when the calcination temperature increases from 900 to 950°C. This last increase in viscosity is possibly due to the improvement of particle–particle interactions inside the SSA and organic additives mixtures, caused not only by a structural changing and an intensification of the crystalline phases developed at high calcination temperatures

Table 3: Fitting parameters of different viscosity rheological models for different TS of SS0 and SSAs at 20°C

Sludge	TS (%)	Cross model					Carreau model				
		$\eta = \eta_\infty + \frac{(\eta_0 - \eta_\infty)}{1 + (\lambda\dot{\gamma})^m}$					$\eta = \eta_\infty + \left[(\eta_0 - \eta_\infty)(1 + (\lambda\dot{\gamma})^2)^{\frac{n-1}{2}}\right]$				
		η_∞ (Pa s)	η_0 (Pa s)	λ (s)	m	R^2	η_∞ (Pa s)	η_0 (Pa s)	λ (s)	n	R^2
SS0	4	1.967×10^{-3}	1.45	11.64	1.15	1.0000	1.547×10^{-3}	1.18	16.01	7.00×10^{-4}	0.9906
	7	2.268×10^{-3}	1.05	14.71	1.00	0.9964	2.288×10^{-3}	0.69	10.10	6.84×10^{-4}	0.9947
	10	2.280×10^{-3}	0.59	13.16	0.95	0.9985	2.336×10^{-3}	0.05	0.71	7.59×10^{-4}	0.9920
	13	2.760×10^{-3}	0.92	11.34	1.01	1.0000	2.760×10^{-3}	0.23	2.93	7.46×10^{-4}	0.9971
	15	3.310×10^{-3}	0.21	3.05	0.97	1.0000	3.372×10^{-3}	0.06	0.78	7.87×10^{-4}	0.9976
SSA800	4	1.208×10^{-3}	0.54	10.85	0.99	1.0000	1.245×10^{-3}	0.10	1.95	7.49×10^{-4}	0.9986
	7	1.444×10^{-3}	0.66	11.49	1.03	0.9989	1.388×10^{-3}	0.20	3.87	5.93×10^{-4}	0.9938
	10	1.587×10^{-3}	0.50	9.26	0.98	1.0000	1.552×10^{-3}	0.05	0.79	7.55×10^{-4}	0.9956
	13	1.982×10^{-3}	0.13	1.98	0.92	1.0000	2.203×10^{-3}	0.04	0.54	9.40×10^{-4}	0.9985
	15	2.264×10^{-3}	0.18	2.08	0.90	1.0000	2.542×10^{-3}	0.07	0.72	7.56×10^{-4}	0.9969
SSA850	4	1.167×10^{-3}	0.16	3.49	0.96	1.0000	1.062×10^{-3}	0.05	1.10	1.15×10^{-4}	0.9897
	7	1.242×10^{-3}	0.43	7.51	1.03	1.0000	1.241×10^{-3}	0.13	2.47	5.89×10^{-4}	0.9979
	10	1.267×10^{-3}	0.41	6.20	1.00	0.9990	1.237×10^{-3}	0.06	0.85	7.56×10^{-4}	0.9881
	13	1.695×10^{-3}	0.20	2.95	0.97	1.0000	1.566×10^{-3}	0.05	0.69	8.01×10^{-4}	0.9941
	15	2.128×10^{-3}	0.11	1.49	0.90	1.0000	1.830×10^{-3}	0.06	0.78	7.29×10^{-4}	0.9918
SSA900	4	1.164×10^{-3}	0.23	3.98	1.04	1.0000	1.250×10^{-3}	0.10	1.90	7.45×10^{-4}	0.9974
	7	1.237×10^{-3}	0.29	4.63	1.05	1.0000	1.202×10^{-3}	0.24	4.75	7.04×10^{-4}	0.9984
	10	1.268×10^{-3}	0.31	6.10	0.95	0.9994	1.394×10^{-3}	0.05	0.87	7.47×10^{-4}	0.9939
	13	1.332×10^{-3}	0.25	3.99	0.96	1.0000	1.418×10^{-3}	0.06	0.86	8.06×10^{-4}	0.9978
	15	1.854×10^{-3}	0.12	1.54	0.90	0.9992	2.480×10^{-3}	0.06	0.76	1.07×10^{-3}	0.9936
SSA950	4	1.162×10^{-3}	0.24	3.90	1.03	1.0000	1.193×10^{-3}	0.10	1.76	9.99×10^{-4}	0.9941
	7	1.233×10^{-3}	0.26	4.26	1.04	0.9995	1.208×10^{-3}	0.24	4.69	9.76×10^{-4}	0.9246
	10	1.248×10^{-3}	0.17	3.96	0.93	0.9993	1.261×10^{-3}	0.04	0.70	1.00×10^{-3}	0.9973
	13	1.355×10^{-3}	0.17	3.01	0.91	1.0000	1.608×10^{-3}	0.05	0.69	1.00×10^{-3}	0.9961
	15	1.361×10^{-3}	0.13	1.65	1.04	0.9997	1.291×10^{-3}	0.05	0.74	1.00×10^{-3}	0.9986

(Figure 2), but also by a competition between weak solid interactions (SSA900 and SSA950) and stronger viscous forces brought by organic additives (proportion: 4% methocel + 4% amijel + 8% starch), which in turn increases the viscosity of the dispersion. The organic additives can act physically and chemically in the system: sewage sludge ash/water, by the modification of the gradients of the chemical and electrical potentials. They formed hydrogels with their three-dimensional (3D) network chains, where the polar or charged hydrophilic parts are solvated by water molecules, but the non-polar hydrophobic parts are chemically or physically linked with each other and adsorbed on the sludge ash particles.

The apparent viscosity (η)−shear rate ($\dot{\gamma}$) experimental data of the first regime were fitted to different rheological models discussed in equations (4)–(6). The various rheological parameters estimated from different models are presented in Table 5, where the Cross and Carreau models were privileged, based on the high values of linear correlation coefficient (R^2), as the best model fitting the experimental data.

According to both models (Cross and Carreau), the increase in SSA and organic additives' TS resulted in an increase of the infinite-shear rate apparent viscosity ($\eta_C = \eta_\infty$). This rise in viscosity is possibly due to the effective homogeneous dispersion of SSA and organic additives mixtures in water, and to the improvement of particle–particle interactions via electrostatic, steric or electrosteric mechanisms, forming a strong structural network [43,78,80]. Furthermore, for TS = 4%, the increase in calcination temperature is accompanied by an increase of the infinite-shear rate apparent viscosity ($\eta_C = \eta_\infty$). This is probably due to the low presence of the mixture dispersed in the water. Above TS = 4%, the infinite-shear rate apparent viscosity ($\eta_C = \eta_\infty$) decreases when the calcination temperature increases from 800 to 850°C, then it increases, respectively, with a big step to reach a maximum value when the calcination temperature increases from 900 to 950°C.

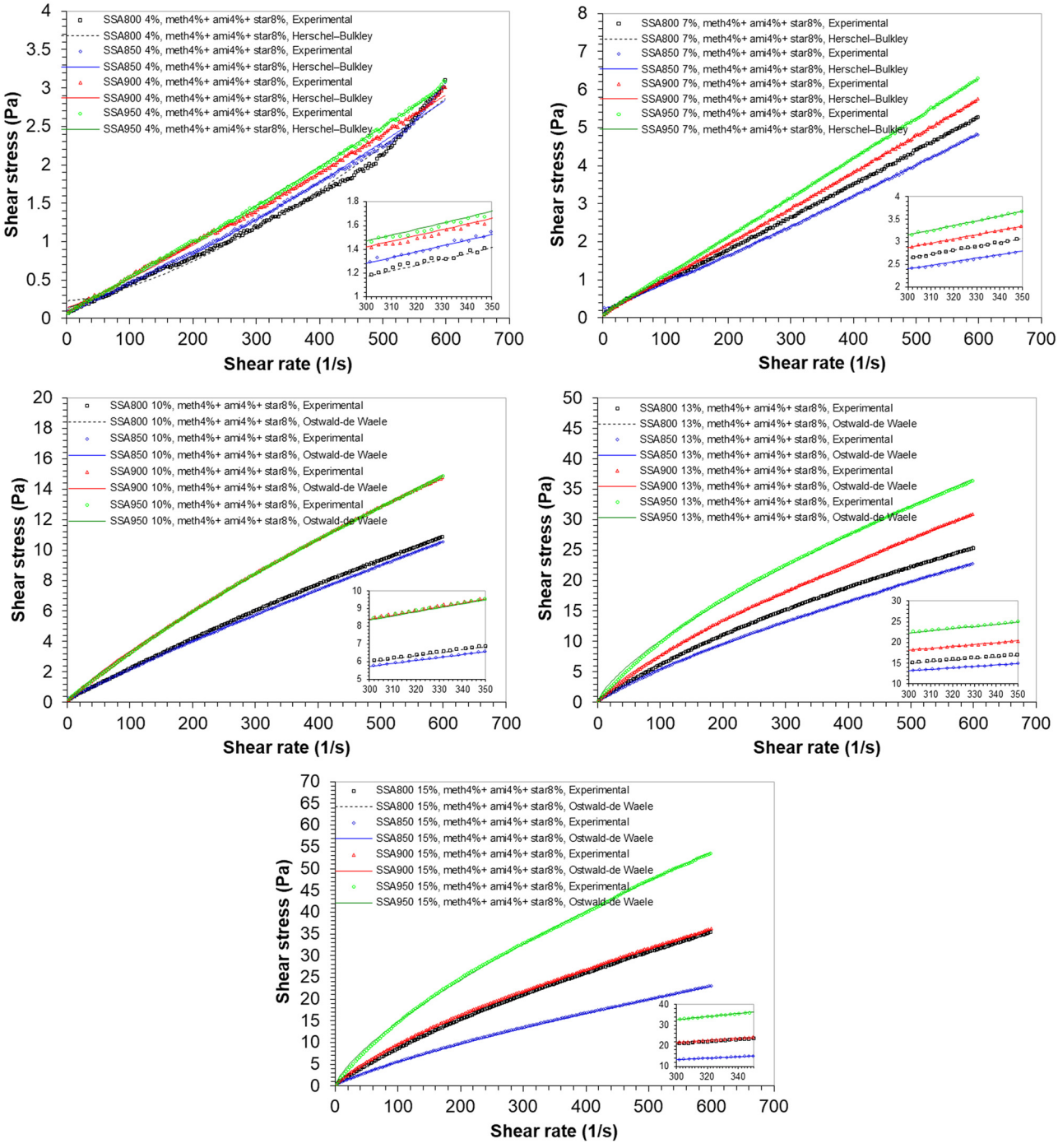

Figure 8: Shear stress (τ)–shear rate ($\dot{\gamma}$) curves of SSAs, mixed with organic additives (4% methocel + 4% amijel + 8% starch), for different TS = 4, 7, 10, 13, and 15%, at 20°C.

3.6.4 Effect of methocel percentage on the rheological behaviour of SSA and organic additive mixtures

Figures 10 and 11, respectively, illustrate the first step shear stress (τ)–shear rate ($\dot{\gamma}$) and apparent viscosity (η)–shear rate ($\dot{\gamma}$) curves with the best-fit rheological model of sewage sludge ash SSA850, mixed with organic additives (4% amijel + 8% starch) and various percentages of methocel: 3, 4, 5, and 6%, for different TS = 4, 7, 10, 13, and 15%, at 20°C.

Figure 10 highlights that for SSA850 and organic additives mixtures, the shear stress increases with increasing

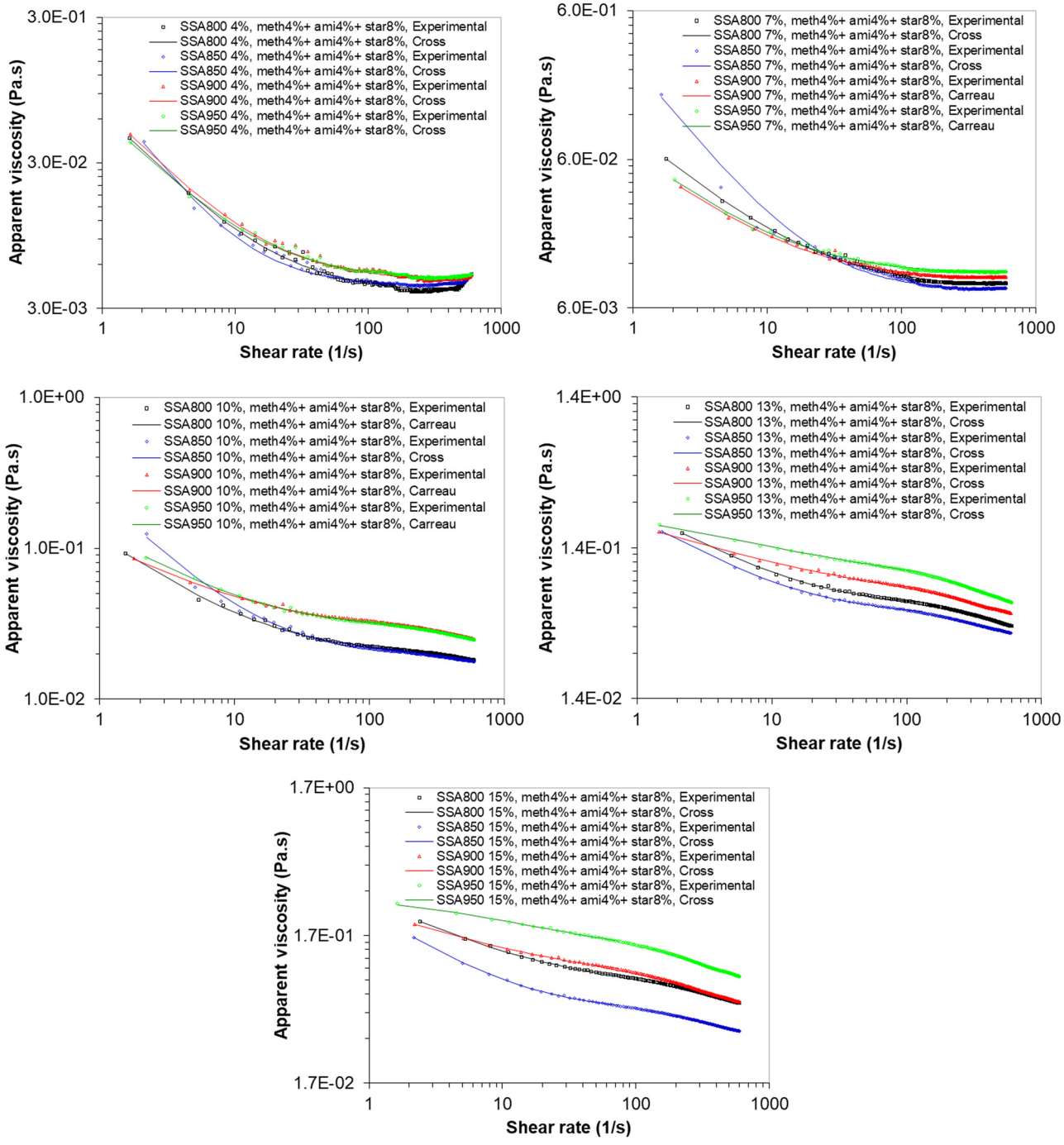

Figure 9: Apparent viscosity (η)–shear rate ($\dot{\gamma}$) curves of SSA, mixed with organic additives (4% methocel + 4% amijel + 8% starch), for different TS = 4, 7, 10, 13, and 15%, at 20°C.

shear rate indicating non-Newtonian shear thickening (yield dilatant) flow behaviour at low TS (4 and 7%) for all methocel percentages and shear-thinning (pseudo-plastic) flow behaviour at high TS (10, 13, and 15%) for methocel percentages of 4, 5, and 6%. It can be remarked from this figure that the shear stress increases significantly when the percentage of methocel increases from 2 to 6%. This means that the increase in organic additives percentage enhances the shear-thinning behaviour and leads to higher shear-stress magnitudes [59,81].

The shear stress (τ)–shear rate ($\dot{\gamma}$) experimental data were fitted to different rheological models discussed in equations (1)–(3). Several rheological parameters estimated from different models are presented with a thixotropic

Table 4: Fitting parameters of different shear stress rheological models for different TS of SSAs mixed with organic additives (4% methocel + 4% amijel + 8% starch) at 20°C

Sludge	TS (%)	Herschel–Bulkley model				Ostwald–de Waele model			Thixotropy
		$\tau = \tau_0 + Ky^n$				$\tau = Ky^n$			
		τ_0 (Pa)	K (Pa s)	n	R^2	K (Pa s)	n	R^2	rHa (Pa s^{-1})
SSA800 + 4% methocel + 4% amijel + 8% starch	4	0.2306	1.96×10^{-4}	1.4864	0.9913	1.50×10^{-3}	1.1813	0.9834	18.87
	7	0.1844	6.21×10^{-3}	1.0490	0.9998	1.08×10^{-2}	0.9665	0.9989	82.19
	10	−0.0500	4.39×10^{-2}	0.8634	0.9998	4.15×10^{-2}	0.8718	0.9998	242.35
	13	−0.7437	2.50×10^{-1}	0.7275	0.9996	1.85×10^{-1}	0.7707	0.9993	525.66
	15	−0.7322	3.12×10^{-1}	0.7432	0.9999	2.51×10^{-1}	0.7746	0.9997	NT
SSA850 + 4% methocel + 4% amijel + 8% starch	4	0.1423	9.44×10^{-4}	1.2445	0.9966	2.54×10^{-3}	1.0953	0.9941	41.14
	7	0.2324	4.64×10^{-3}	1.0786	0.9997	1.02×10^{-2}	0.9613	0.9978	69.48
	10	0.0738	3.54×10^{-2}	0.8898	0.9999	3.88×10^{-2}	0.8764	0.9999	175.48
	13	−0.3084	1.64×10^{-1}	0.7735	0.9999	1.41×10^{-1}	0.7952	0.9998	241.47
	15	−0.3487	1.73×10^{-1}	0.7659	0.9999	1.47×10^{-1}	0.7900	0.9998	NT
SSA900 + 4% methocel + 4% amijel + 8% starch	4	0.1372	2.29×10^{-3}	1.1097	0.9987	5.10×10^{-3}	0.9891	0.9968	58.18
	7	0.1416	7.57×10^{-3}	1.0329	0.9999	1.11×10^{-2}	0.9756	0.9994	58.77
	10	−0.2419	8.86×10^{-2}	0.8036	0.9998	7.35×10^{-2}	0.8310	0.9997	268.27
	13	−0.4811	2.66×10^{-1}	0.7452	0.9998	2.26×10^{-1}	0.7690	0.9997	233.02
	15	−0.7838	3.96×10^{-1}	0.7082	0.9999	3.19×10^{-1}	0.7394	0.9997	NT
SSA950 + 4% methocel + 4% amijel + 8% starch	4	0.1230	2.42×10^{-3}	1.1084	0.9993	4.80×10^{-3}	1.0048	0.9979	56.79
	7	0.1301	8.77×10^{-3}	1.0246	0.9999	1.21×10^{-2}	0.9770	0.9996	58.35
	10	−0.2068	8.23×10^{-2}	0.8149	0.9998	6.99×10^{-2}	0.8387	0.9997	219.88
	13	−1.4948	5.41×10^{-1}	0.6644	0.9997	3.70×10^{-1}	0.7185	0.9991	NT
	15	−1.4462	6.94×10^{-1}	0.6836	0.9997	5.36×10^{-1}	0.7205	0.9995	NT

area (rHa) in Table 6, where the Herschel–Bulkley and Ostwald–de Waele models were preferred, referring to the high values of linear correlation coefficient (R^2) and the physical meaning, as the best models fitting the experimental data. According to Herschel–Bulkley and Ostwald–de Waele models, for each TS, the increase in the methocel percentage caused roughly a decrease in flow behaviour index (n) and an increase in flow consistency coefficient (K).

As expected from Table 6, SSA850 and organic additives mixtures containing 3, 5, and 6% of methocel exhibit a non-thixotropic behaviour. This alteration in behaviour (non-thixotropy) occurs at the cross-over point of the shear-rate-rising (continuous ramp step 1) and shear-rate-falling (continuous ramp step 2) for methocel percentages of 3 and 5%. However, for a methocel percentage of 6%, the non-thixotropy occurs while the shear-rate-falling is greater than the shear-rate-rising.

Figure 11 compares different TS, the viscosity behaviour of SSA850 and organic additives mixtures, as the methocel percentage varies from 3 to 6%, and an applied shear rate increases from 0 to 600 s^{-1}. For a low methocel percentage (3%), the apparent viscosity exhibits similar behaviours as that detected for SS0 and SSA (shear-thinning laminar and shear-thickening turbulent behaviours, Figure 6). However, for methocel percentages above 3% (4–6%), the shear rate dependence of the apparent viscosity reveals a shear-thinning flow behaviour. As also reported in Figure 11, it could be stated that for all TS, the apparent viscosity increases with the increase of the methocel percentage. The viscosity rheological parameters estimated from different models are presented in Table 7, where the Cross model was preferred as the best model fitting the experimental data.

According to the Cross model, the increase in the methocel percentage resulted in an increase of the infinite-shear rate apparent viscosity ($\eta_C = \eta_\infty$). This interesting increase in viscosity is due to the primordial role of the plasticizer (methocel), which makes it possible to extend the pseudo-plastic plateau by reducing the migration of the liquid phase [82–84]. Plasticizers are adsorbed on the surface of SSA particles and, depending on their chemistry, create surface charges participating in the electrostatic repulsion of the SSA particles [85] or form deposits covering the particles' morphology and allowing better relative sliding of these last ones. In addition, plasticizers can also attach water molecules to their chains, thus creating a water-saturated network which in turn facilitates the sliding of particles over each other [82,86].

Table 5: Fitting parameters of different viscosity rheological models for different TS of SSA, mixed with organic additives (4% methocel + 4% amijel + 8% starch), at 20°C

Sludge	TS (%)	Cross model					Carreau model				
		$\eta = \eta_\infty + \frac{(\eta_0 - \eta_\infty)}{1 + (\lambda\dot{\gamma})^m}$					$\eta = \eta_\infty + \left[(\eta_0 - \eta_\infty)(1 + (\lambda\dot{\gamma})^2)^{\frac{n-1}{2}}\right]$				
		η_∞ (Pa s)	η_0 (Pa s)	λ (s)	M	R^2	η_∞ (Pa s)	η_0 (Pa s)	λ (s)	n	R^2
SSA800 + 4% methocel + 4% amijel + 8% starch	4	3.810×10^{-3}	0.85	12.26	1.00	0.9979	3.817×10^{-3}	0.16	2.31	1.79×10^{-4}	0.9968
	7	8.071×10^{-3}	0.86	14.64	0.84	1.0000	8.517×10^{-3}	0.09	0.62	1.80×10^{-4}	0.9939
	10	1.926×10^{-2}	0.55	6.38	0.80	0.9960	1.891×10^{-2}	0.70	12.89	2.59×10^{-1}	0.9978
	13	5.496×10^{-2}	0.65	2.61	0.79	1.0000	5.317×10^{-2}	0.42	2.19	3.10×10^{-1}	0.9987
	15	7.422×10^{-2}	0.81	3.71	0.67	0.9994	8.580×10^{-2}	0.24	0.31	1.80×10^{-4}	0.9963
SSA850 + 4% methocel + 4% amijel + 8% starch	4	4.300×10^{-3}	1.09	6.89	1.27	0.9830	3.981×10^{-3}	1.02	14.38	2.89×10^{-4}	0.9289
	7	7.752×10^{-3}	3.35	8.90	1.15	0.9955	6.991×10^{-3}	1.67	7.13	6.72×10^{-5}	0.9687
	10	1.854×10^{-2}	1.66	7.90	0.96	1.0000	1.862×10^{-2}	1.22	5.38	1.53×10^{-4}	0.9993
	13	4.781×10^{-2}	0.75	4.33	0.77	1.0000	4.644×10^{-2}	0.42	2.82	3.13×10^{-1}	0.9996
	15	5.021×10^{-2}	0.82	3.85	0.83	0.9996	4.868×10^{-2}	0.55	3.29	2.55×10^{-1}	0.9983
SSA900 + 4% methocel + 4% amijel + 8% starch	4	4.583×10^{-3}	1.27	17.48	1.00	1.0000	4.587×10^{-3}	0.23	3.22	1.01×10^{-4}	0.9969
	7	9.014×10^{-3}	0.25	4.63	0.83	0.9947	8.943×10^{-3}	0.10	1.77	2.13×10^{-1}	1.0000
	10	2.785×10^{-2}	0.59	15.98	0.65	0.9971	2.743×10^{-2}	0.21	3.76	3.94×10^{-1}	0.9994
	13	5.656×10^{-2}	0.78	24.11	0.45	0.9982	5.279×10^{-2}	0.30	3.92	6.13×10^{-1}	0.9973
	15	8.044×10^{-2}	0.56	3.13	0.56	1.0000	7.369×10^{-2}	0.30	1.68	5.63×10^{-1}	0.9985
SSA950 + 4% methocel + 4% amijel + 8% starch	4	4.731×10^{-3}	0.99	16.60	0.99	1.0000	4.699×10^{-3}	0.96	18.22	3.79×10^{-2}	0.9961
	7	9.989×10^{-3}	0.30	5.34	0.85	0.9962	9.926×10^{-3}	0.15	2.78	1.91×10^{-1}	0.9991
	10	2.770×10^{-2}	0.50	6.80	0.72	0.9983	2.831×10^{-2}	0.12	0.63	2.34×10^{-1}	0.9984
	13	5.708×10^{-2}	0.51	6.68	0.35	1.0000	3.861×10^{-2}	0.31	6.91	7.69×10^{-1}	0.9988
	15	1.108×10^{-1}	0.34	0.15	0.60	0.9965	6.329×10^{-2}	0.30	0.67	7.64×10^{-1}	0.9953

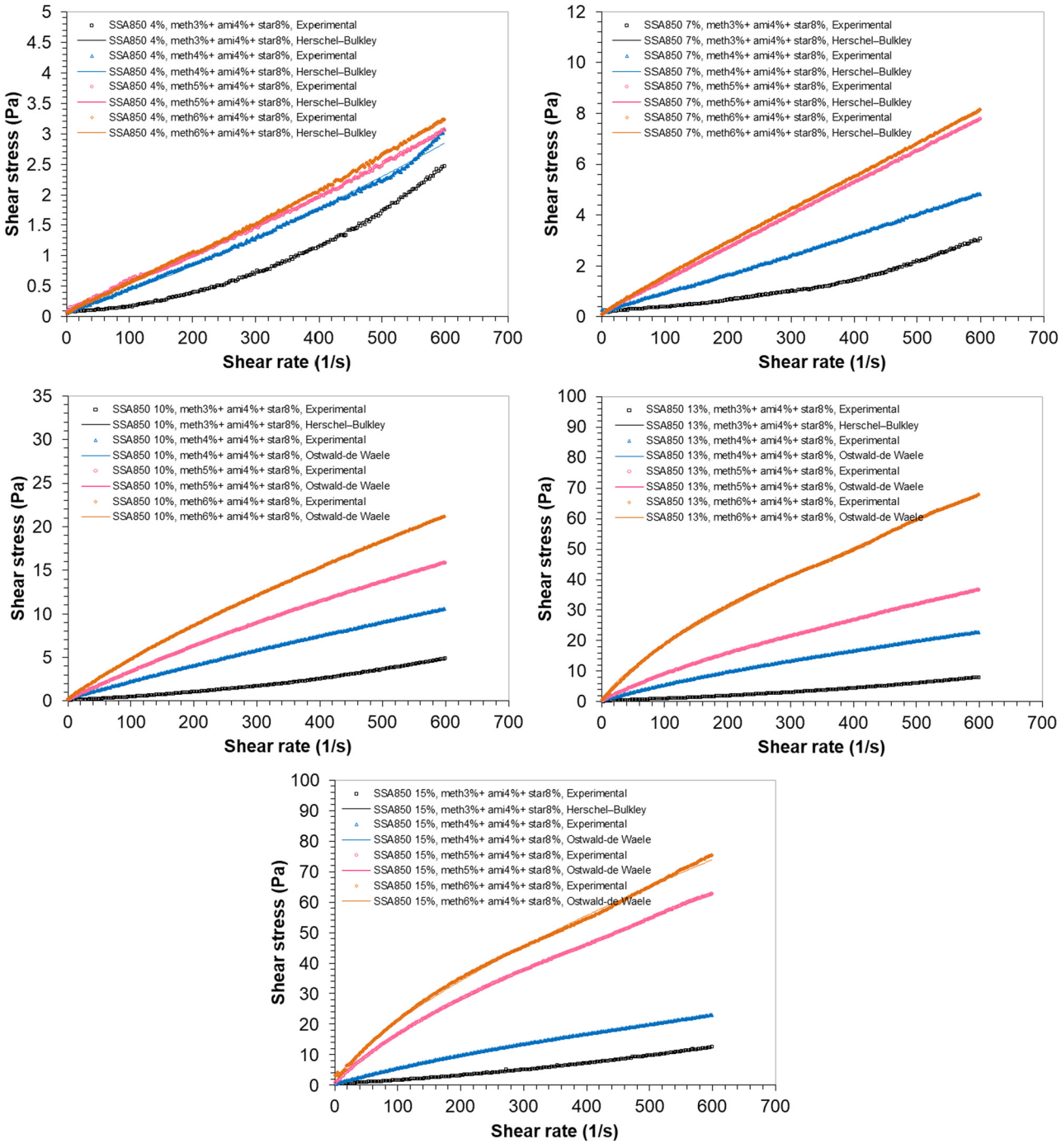

Figure 10: Shear stress (τ)–shear rate ($\dot{\gamma}$) curves of sewage sludge ash SSA850, mixed with organic additives (4% amijel + 8% starch) and various percentages of methocel: 3, 4, 5, and 6%, for different TS, at 20°C.

3.6.5 Effect of testing temperature on the rheological behaviour of sludge systems

The effect of temperature on rheological properties of different sludge systems (SS0, SSA850, SSA850 mixed with 4% methocel + 4% amijel + 8% starch, and SSA850 mixed with 5% methocel + 4% amijel + 8% starch) has been studied at different testing temperatures of 20, 30, 40, 50, and 60°C for a TS of 10%. As shown in Figures 12 and 13, experimental results show that temperature exerted a significant impact on the shear stress (τ)–shear rate ($\dot{\gamma}$) and apparent viscosity (η)–shear rate ($\dot{\gamma}$) curves over the entire temperature range (20–60°C).

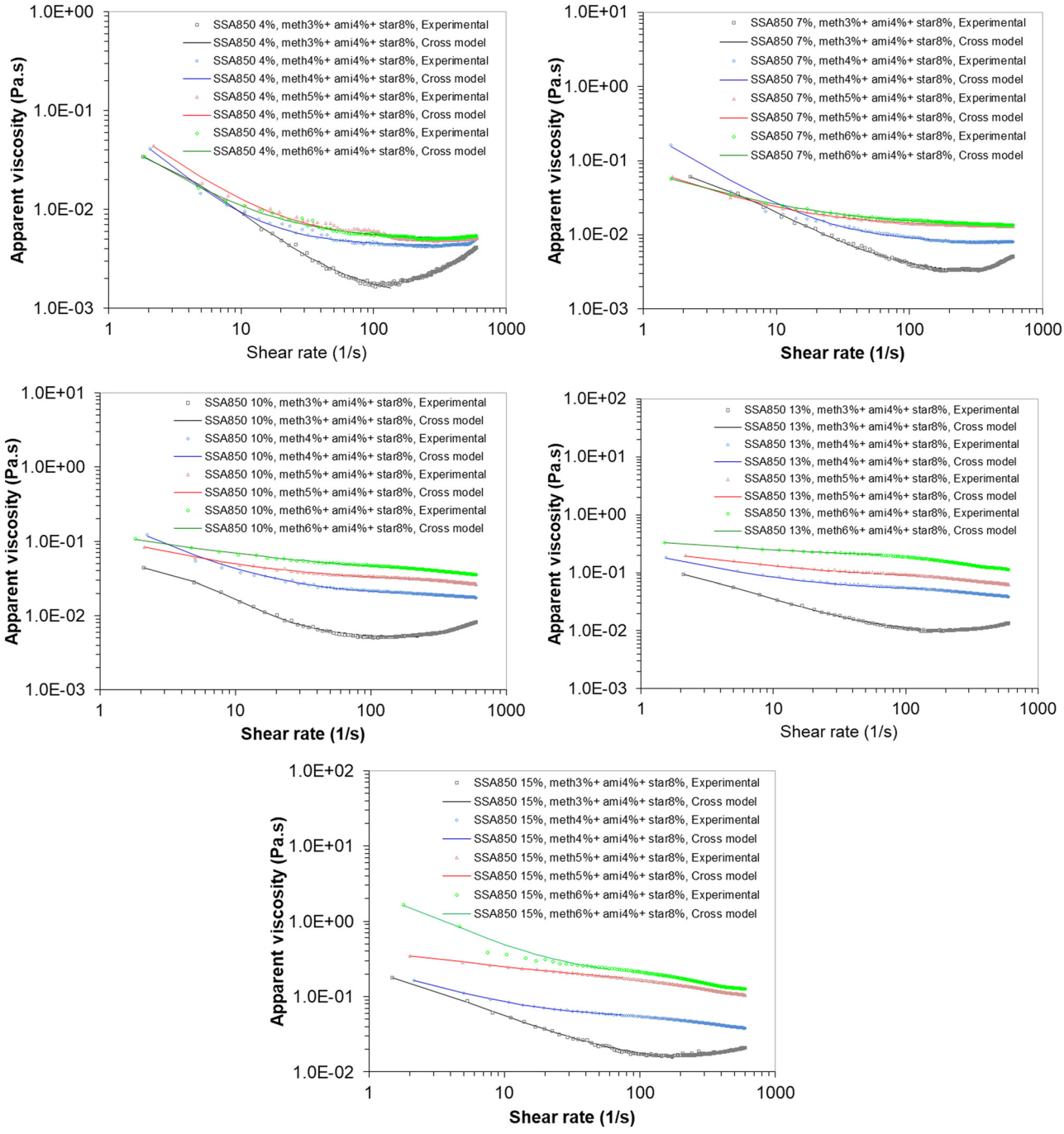

Figure 11: Apparent viscosity (η)–shear rate ($\dot{\gamma}$) curves of sewage sludge ash SSA850, mixed with organic additives (4% amijel + 8% starch) and various percentages of methocel: 3, 4, 5, and 6%, for different TS, at 20°C.

Figure 12 reports that for all testing temperatures, the shear stress increases with increasing shear rate, indicating non-Newtonian shear thickening (yield dilatant) flow behaviour for SS0 and SSA850 and shear-thinning (pseudoplastic) for SSA850 mixed with 4% methocel + 4% amijel + 8% starch, and SSA850 mixed with 5% methocel + 4% amijel + 8% starch. As can be obviously observed in this figure, the shear stress decreases meaningfully when the testing temperature increases from 20 to 60°C. This decrease is the result of the thermal destruction of sludge systems, which manifests itself in the reduction of the mutual interaction between particles [42,52,58,85,87].

As also mentioned in Table 8, only the sludge system composed of SSA850 mixed with 4% methocel + 4% amijel

Table 6: Fitting parameters of different shear stress rheological models for different TS of SSA850, mixed with organic additives (4% amijel + 8% starch) and various percentages of methocel: 3, 4, 5, and 6%, at 20°C

Sludge	TS (%)	Herschel–Bulkley model				Ostwald–de Waele model			Thixotropy
		$\tau = \tau_0 + Ky^n$				$\tau = Ky^n$			
		τ_0 (Pa)	K (Pa s)	n	R^2	K (Pa s)	n	R^2	rHa (Pa s^{-1})
SSA850 + 3% methocel + 4% amijel + 8% starch	4	0.1117	7.97×10^{-6}	1.9683	0.9993	3.97×10^{-5}	1.7211	0.9949	NT
	7	0.3205	6.56×10^{-6}	2.0215	0.9956	3.06×10^{-4}	1.4294	0.9728	NT
	10	0.2465	1.42×10^{-4}	1.6243	0.9990	5.79×10^{-4}	1.4091	0.9950	NT
	13	0.5263	5.27×10^{-4}	1.4941	0.9991	2.69×10^{-3}	1.2460	0.9932	NT
	15	0.7269	1.54×10^{-3}	1.3971	0.9993	5.78×10^{-3}	1.1968	0.9951	NT
SSA850 + 4% methocel + 4% amijel + 8% starch	4	0.1423	9.44×10^{-4}	1.2445	0.9966	2.54×10^{-3}	1.0953	0.9941	41.14
	7	0.2324	4.64×10^{-3}	1.0786	0.9997	1.02×10^{-2}	0.9613	0.9978	69.48
	10	0.0738	3.54×10^{-2}	0.8898	0.9999	3.88×10^{-2}	0.8764	0.9999	175.48
	13	−0.3084	1.64×10^{-1}	0.7735	0.9999	1.41×10^{-1}	0.7952	0.9998	241.47
	15	−0.3487	1.73×10^{-1}	0.7659	0.9999	1.47×10^{-1}	0.7900	0.9998	NT
SSA850 + 5% methocel + 4% amijel + 8% starch	4	0.1618	2.10×10^{-3}	1.1285	0.9990	5.31×10^{-3}	0.9897	0.9966	NT
	7	0.1035	1.47×10^{-2}	0.9779	1.0000	1.79×10^{-2}	0.9491	0.9998	NT
	10	−0.2135	8.02×10^{-2}	0.8297	0.9998	6.83×10^{-2}	0.8531	0.9997	NT
	13	−0.5515	2.97×10^{-1}	0.7552	0.9999	2.53×10^{-1}	0.7786	0.9998	NT
	15	−0.9060	6.48×10^{-1}	0.7163	0.9997	5.60×10^{-1}	0.7374	0.9996	NT
SSA850 + 6% methocel + 4% amijel + 8% starch	4	0.1208	2.15×10^{-3}	1.1360	0.9993	4.42×10^{-3}	1.0284	0.9979	NT
	7	0.1226	1.78×10^{-2}	0.9539	0.9999	2.21×10^{-2}	0.9220	0.9997	NT
	10	−0.0702	1.20×10^{-1}	0.8106	0.9999	1.05×10^{-1}	0.8304	0.9999	NT
	13	−0.2255	8.35×10^{-1}	0.6900	0.9993	6.70×10^{-1}	0.7215	0.9991	NT
	15	−0.7781	8.19×10^{-1}	0.7039	0.9985	8.26×10^{-1}	0.7025	0.9985	NT

+ 8% starch exhibited a thixotropic response at testing temperatures of 20, 30 and 40°C. With the increase of temperature from 20 to 40°C, the rHa decreased gradually from 175.48 to 59.04 Pa s^{-1}. This indicates that the thixotropic behaviour of the sludge system was distinctly weakened during the heating testing. Thus highlighting that temperature negatively impacts the network strength between the particles and breaking some chemical bonds of macromolecules. The more aggregated particles can be fractured, the size and fraction of particles be reduced, and solid matter dissolves into liquid [81].

The shear stress–shear rate rheograms were found to best fit the Herschel–Bulkley model. The several rheological parameters extracted from different models are collected with the thixotropic area (rHa) in Table 8. For all sludge systems, conforming to the Herschel–Bulkley model, an increase in testing temperature usually brings about a decrease in yield stress (τ_0).

The relationship between sludge systems' apparent viscosity and temperature is exposed in Figure 13. On the whole testing temperature range (20–60°C), the viscosity decreased with the increasing temperature due to the weakening of inter-molecular cohesive forces within the sludge systems. For all testing temperatures, the apparent viscosity of SS0 and SSA850 systems exhibit shear-thinning laminar and shear-thickening turbulent behaviours. Furthermore, for the systems composed of SSA850 mixed with 4% methocel + 4% amijel + 8% starch, and SSA850 mixed with 5% methocel + 4% amijel + 8% starch, the shear rate dependence of the apparent viscosity discloses a shear-thinning flow behaviour.

Moreover, different rheological models were fitted to the apparent viscosity (η)–shear rate ($\dot{\gamma}$) curves, and the obtained rheological parameters are tabulated in Table 9. According to Cross and Carreau models, the increase in testing temperature induced a decrease of the infinite-shear rate apparent viscosity ($\eta_C = \eta_\infty$). This decrease in infinite-rate viscosity is due to some restructuring in the sludge systems network, which resulted in the weakening of the network strength [42,52,58,81,85,87].

3.6.6 Relationship between activation energy and apparent viscosity of sludge systems

In general, the activation energy signifies the strength of the inter-particle forces that preserve the cohesion of the sludge system network. An increase in activation energy reveals higher resistance to flow and greater sludge network strength [56–58,81].

Table 7: Fitting parameters of different viscosity rheological models for different TS of SSA850, mixed with organic additives (4% amijel + 8% starch) and various percentages of methocel: 3, 4, 5, and 6%, at 20°C

Sludge	TS (%)	Cross model					Carreau model				
		$\eta = \eta_\infty + \frac{(\eta_0 - \eta_\infty)}{1 + (\lambda\dot{\gamma})^m}$					$\eta = \eta_\infty + \left[(\eta_0 - \eta_\infty)(1 + (\lambda\dot{\gamma})^2)^{\frac{n-1}{2}}\right]$				
		η_∞ (Pa s)	η_0 (Pa s)	λ (s)	m	R^2	η_∞ (Pa s)	η_0 (Pa s)	λ (s)	n	R^2
SSA850 + 3% methocel + 4% amijel + 8% starch	4	1.246×10^{-3}	0.06	0.43	1.24	0.9992	8.456×10^{-4}	0.05	0.56	7.58×10^{-4}	0.9987
	7	2.807×10^{-3}	0.12	0.45	1.16	0.9978	2.461×10^{-3}	0.09	0.49	7.48×10^{-4}	0.9976
	10	4.982×10^{-3}	0.06	0.22	1.55	0.9977	4.184×10^{-3}	0.06	0.44	7.60×10^{-4}	0.9910
	13	8.075×10^{-3}	0.20	0.59	1.00	0.9998	8.489×10^{-3}	0.12	0.40	7.59×10^{-4}	0.9982
	15	1.126×10^{-2}	0.49	1.35	0.87	1.0000	1.359×10^{-2}	0.21	0.46	7.60×10^{-4}	0.9986
SSA850 + 4% methocel + 4% amijel + 8% starch	4	4.300×10^{-3}	1.09	6.89	1.27	0.9830	3.981×10^{-3}	1.02	14.38	2.89×10^{-4}	0.9289
	7	7.752×10^{-3}	3.35	8.90	1.15	0.9955	6.991×10^{-3}	1.67	7.13	6.72×10^{-5}	0.9687
	10	1.854×10^{-2}	1.66	7.90	0.96	1.0000	1.862×10^{-2}	1.22	5.38	1.53×10^{-4}	0.9993
	13	4.781×10^{-2}	0.75	4.33	0.77	1.0000	4.644×10^{-2}	0.42	2.82	3.13×10^{-1}	0.9996
	15	5.021×10^{-2}	0.82	3.85	0.83	0.9996	4.868×10^{-2}	0.55	3.29	2.55×10^{-1}	0.9983
SSA850 + 5% methocel + 4% amijel + 8% starch	4	4.855×10^{-3}	0.97	9.13	1.06	0.9921	4.746×10^{-3}	3.09	37.33	4.51×10^{-4}	0.9909
	7	1.260×10^{-2}	1.15	29.54	0.81	0.9985	1.306×10^{-2}	0.08	0.65	1.50×10^{-4}	0.9894
	10	2.762×10^{-2}	0.79	28.88	0.62	0.9974	3.043×10^{-2}	0.09	0.29	5.00×10^{-4}	0.9701
	13	7.697×10^{-2}	0.42	1.32	0.65	1.0000	6.880×10^{-2}	0.64	13.86	5.48×10^{-1}	0.9983
	15	1.231×10^{-1}	0.71	1.39	0.49	0.9995	1.732×10^{-1}	0.36	0.21	1.01×10^{-4}	0.9817
SSA850 + 6% methocel + 4% amijel + 8% starch	4	4.993×10^{-3}	0.47	8.62	0.98	0.9944	5.025×10^{-3}	0.08	1.36	7.45×10^{-4}	0.9923
	7	1.284×10^{-2}	0.86	42.80	0.69	1.0000	1.278×10^{-2}	0.20	5.28	3.29×10^{-1}	0.9979
	10	3.261×10^{-2}	0.63	44.98	0.45	0.9968	3.190×10^{-2}	0.19	3.67	5.89×10^{-1}	0.9916
	13	1.637×10^{-1}	0.68	3.48	0.46	0.9991	1.466×10^{-1}	0.42	2.20	6.86×10^{-1}	0.9988
	15	2.536×10^{-1}	1.82	0.26	2.99	0.9937	1.771×10^{-1}	2.75	0.80	4.43×10^{-4}	0.9915

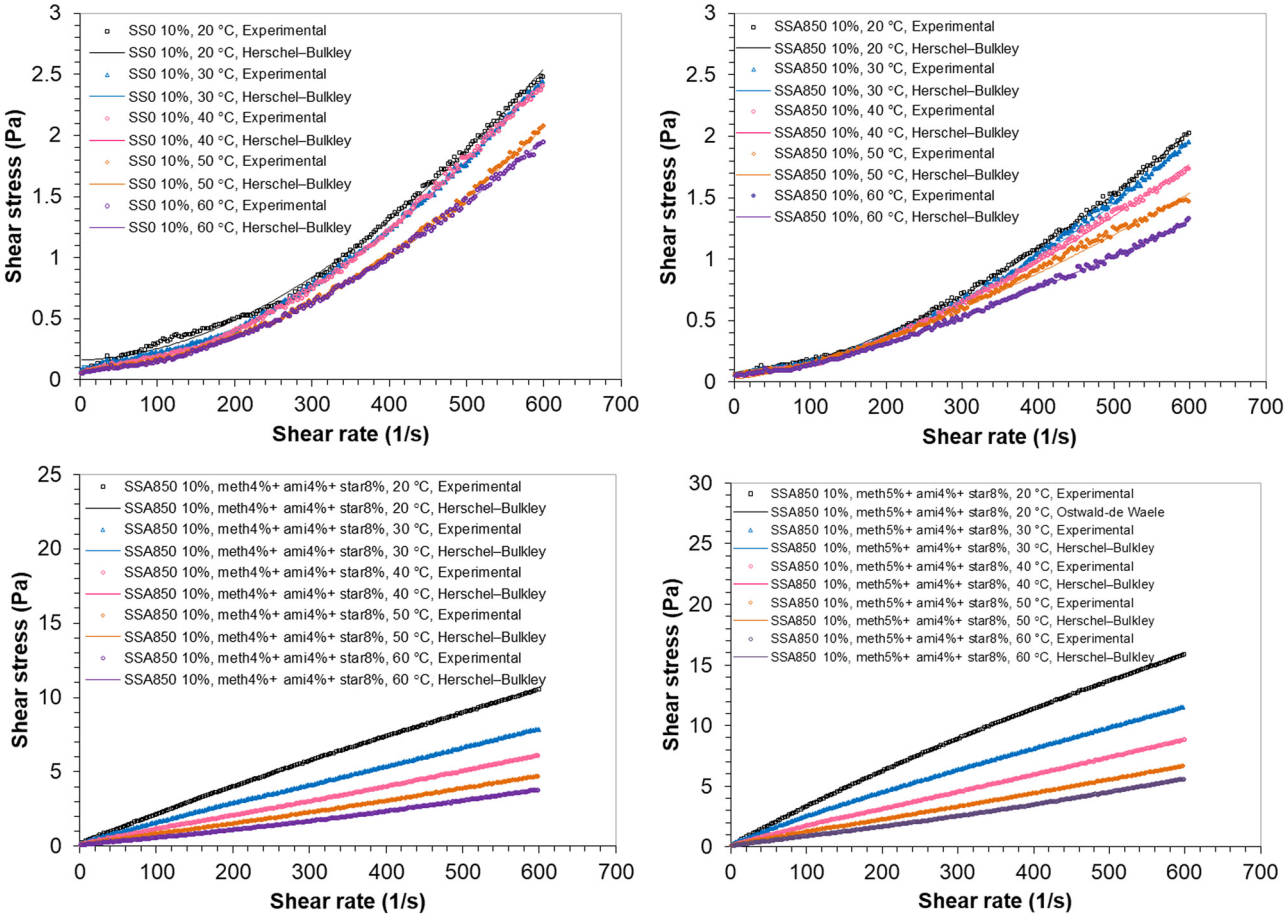

Figure 12: Shear stress (τ)–shear rate ($\dot{\gamma}$) curves of sludge systems (SS0, SSA850, SSA850 + 4% methocel + 4% amijel + 8% starch, and SSA850 + 5% methocel + 4% amijel + 8% starch) for a TS = 10%, at different testing temperatures (20, 30, 40, 50, and 60°C).

The dependence between temperature and apparent viscosity of different sludge systems (SS0, SSA850, SSA850 + 4% methocel + 4% amijel + 8% starch, and SSA850 + 5% methocel + 4% amijel + 8% starch), at a TS of 10%, can be commonly expressed by the Arrhenius model equation:

$$\ln \eta_\infty = \ln \eta_0 + \frac{E_a}{RT}, \tag{7}$$

where η_∞ is the infinite-shear rate apparent viscosity (Pa s), η_0 is the zero-shear rate apparent viscosity (Pa s) (generally termed the frequency factor: pre-exponent coefficient), E_a is the activation energy (J mol^{-1}), R is the universal gas constant (8.314 J mol^{-1} K^{-1}), and T is the absolute temperature (K).

The activation energies and the zero-shear rate apparent viscosities of the flow process were calculated, respectively, from the slope and the intercept of the Arrhenius-type plots (ln η_∞ against 1/T) as shown in Figure 14, and the obtained values are presented in Table 10.

It shows that the sludge system composed of SSA850 mixed with 5% methocel + 4% amijel + 8% starch exhibits the highest activation energy (24.67 kJ mol^{-1}) followed by the system consisting of SSA850 mixed with 4% methocel + 4% amijel + 8% starch (23.35 kJ mol^{-1}), then the SS0 system (20.80 kJ mol^{-1}) and lastly the SSA850 system (5.10 kJ mol^{-1}). The activation energies obtained for SS0 and SSA850 mixed with organic additive systems are in the same order of magnitude and compared to those obtained by Hong et al. [56], Gienau et al. [57], and Liu et al. [88], respectively, for municipal TEAS (13.10–24.80 kJ mol^{-1}), for anaerobic sludge obtained from agricultural and bio-waste biogas plants (13.00–20.00 kJ mol^{-1}), and for swine manure (composed of protein, polysaccharide, volatile fatty acids, lignin, etc.)/sewage sludge systems (13.91–25.91 kJ mol^{-1}). The activation energies are also found to be significantly higher than those obtained by Trávníček and Junga [89] for non-diluted (8.87 kJ mol^{-1}) and diluted (9.41–11.56 kJ mol^{-1}) sewage sludge. The activation energy measured for the SSA850 system was proven to be lower than that reported

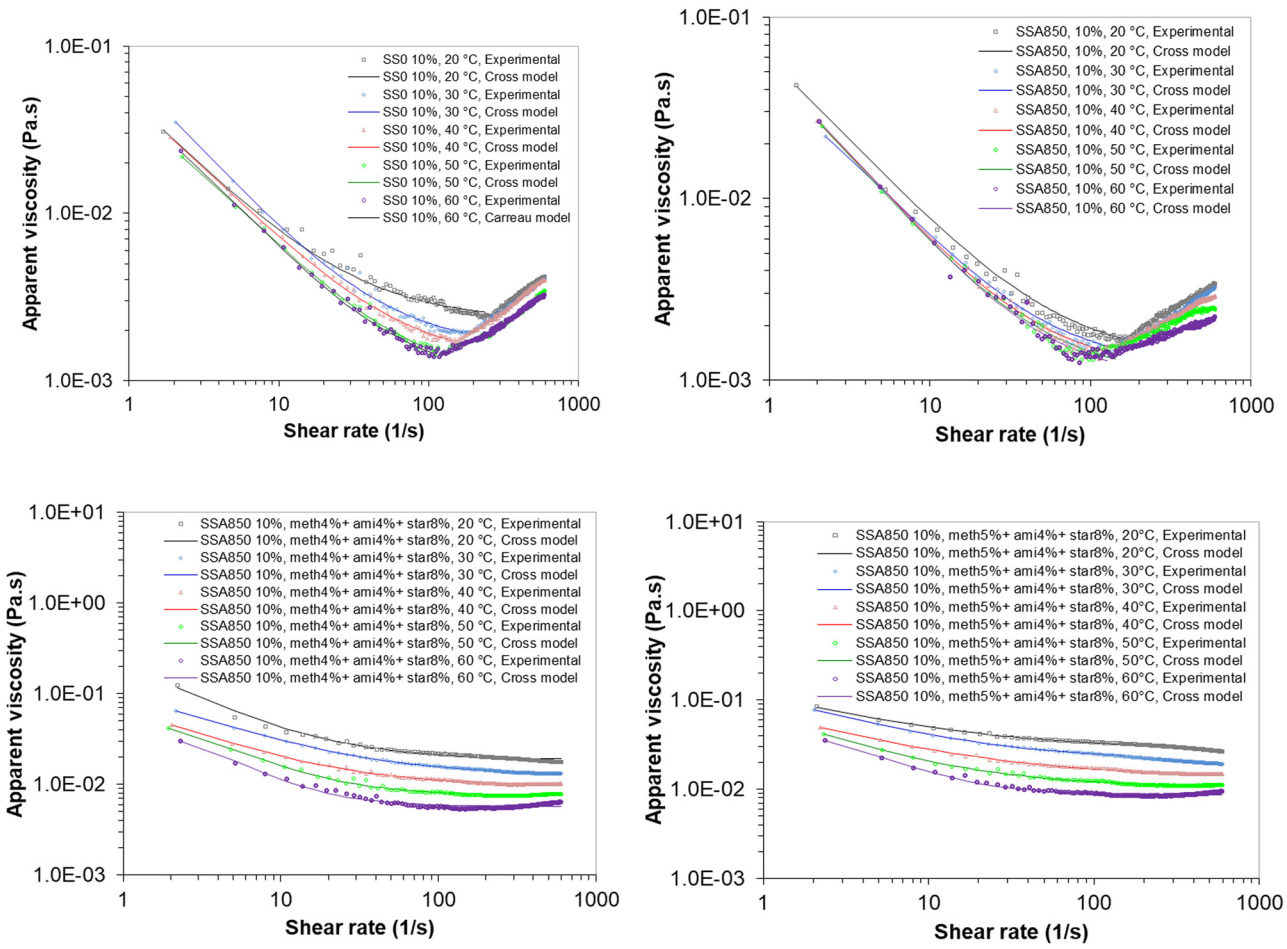

Figure 13: Apparent viscosity (η)−shear rate ($\dot{\gamma}$) curves of sludge systems (SS0, SSA850, SSA850 + 4% methocel + 4% amijel + 8% starch, and SSA850 + 5% methocel + 4% amijel + 8% starch) for a TS = 10%, at different testing temperatures (20, 30, 40, 50, and 60°C).

by Lopez et al. [90] for the activated sludge in MBR (17.69 kJ mol^{-1}).

Through the results presented in Table 10, it can be deduced that, on the one side, the increase of calcination temperature to 850°C induces a sharp decrease in the activation energy from SS0 to SSA850 suspensions, where the apparent viscosity curves shifted to lower levels of viscosity (Figure 7 and Table 9). The reduction of sludge viscosity can be achieved by reduction of its interfacial tension [91]. The observed decrease in the activation energy is due to a combination of devolatilization of organic matter and the transformation of inorganic matter. Indeed, due to the effect of thermal calcination, the overall organic matter content is removed, the oxygen is consumed during the oxidation to form vacancies, and the SSA850 structure underwent modifications such as the transformation of calcite ($CaCO_3$) into lime (CaO). Therefore, the gases generated by the decomposition of minerals and organic additives must pass through the very fine and tortuous porosity to escape from the aggregate [92]. These synergistic effects can be manifested in the increase of the average pore diameter and nanoscale surface roughness of SSA850 particles [93].

On the other side, the addition of organic additives and the increase of methocel percentage to 5% lead to an increase in activation energy caused by the modification of the interaction mechanisms/pathways. This increase can be related to the strong solubilization of organic additives during the thermal treatment, which induced a transfer of the organic matter from the solid compounds to the dissolved constituents, and this transfer is proportional to the evolutions of the yield stress and viscosity [87]. The colloidal sludge suspensions (CSS) are generally stabilized by adsorption of organic compounds on their surface [94–97]. The enhanced stability of CSS with organic coatings has stereotypically been attributed to steric hindrance effects when compressed or deformed adsorbed organic layers overlap and exhibit nonuniform or incomplete

Table 8: Fitting parameters of different shear stress rheological models for a TS = 10% of SS0, SSA850, SSA850 mixed with 4% methocel + 4% amijel + 8% starch, and SSA850 mixed with 5% methocel + 4% amijel + 8% starch, at different testing temperatures (20, 30, 40, 50, and 60°C)

Sludge system	T (°C)	Herschel–Bulkley model				Ostwald–de Waele model			Thixotropy
		$\tau = \tau_0 + Ky^n$				$\tau = Ky^n$			
		τ_0 (Pa)	K (Pa s)	n	R^2	K (Pa s)	n	R^2	rHa (Pa s^{-1})
SS0	20	0.1628	2.15×10^{-5}	1.8161	0.9976	1.61×10^{-4}	1.5076	0.9900	NT
	30	0.1128	1.63×10^{-5}	1.8572	0.9994	7.16×10^{-5}	1.6296	0.9953	NT
	40	0.0846	2.03×10^{-5}	1.8243	0.9992	6.01×10^{-5}	1.6581	0.9969	NT
	50	0.0836	1.29×10^{-5}	1.8677	0.9994	4.85×10^{-5}	1.6638	0.9962	NT
	60	0.0661	2.64×10^{-5}	1.7487	0.9993	7.23×10^{-5}	1.5945	0.9972	NT
SSA850	20	0.0698	5.63×10^{-5}	1.6359	0.9992	1.44×10^{-4}	1.4926	0.9972	NT
	30	0.0609	3.92×10^{-5}	1.6861	0.9993	9.55×10^{-5}	1.5501	0.9976	NT
	40	0.0397	1.04×10^{-4}	1.5204	0.9986	1.81×10^{-4}	1.4354	0.9979	NT
	50	0.0275	1.96×10^{-4}	1.3989	0.9973	2.93×10^{-4}	1.3383	0.9969	NT
	60	0.0409	1.75×10^{-4}	1.3898	0.9986	3.52×10^{-4}	1.2838	0.9973	NT
SSA850 + 4% methocel + 4% amijel + 8% starch	20	0.0738	3.54×10^{-2}	0.8898	0.9999	3.88×10^{-2}	0.8764	0.9999	175.48
	30	0.2021	1.60×10^{-2}	0.9644	0.9998	2.31×10^{-2}	0.9095	0.9994	111.92
	40	0.2005	6.94×10^{-3}	1.0533	0.9996	1.18×10^{-2}	0.9743	0.9988	59.04
	50	0.1598	3.74×10^{-3}	1.1101	0.9997	1.57×10^{-4}	0.0039	0.9987	NT
	60	0.1398	1.31×10^{-3}	1.2387	0.9997	2.72×10^{-3}	1.1293	0.9983	NT
SSA850 + 5% methocel + 4% amijel + 8% starch	20	−0.2135	8.02×10^{-2}	0.8297	0.9998	6.83×10^{-2}	0.8531	0.9997	NT
	30	0.0962	4.32×10^{-2}	0.8711	1.0000	4.81×10^{-2}	0.8554	0.9999	NT
	40	0.1929	1.61×10^{-2}	0.9813	0.9998	2.23×10^{-2}	0.9333	0.9995	NT
	50	0.1875	8.13×10^{-3}	1.0435	0.9998	1.27×10^{-2}	0.9767	0.9991	NT
	60	0.2102	2.52×10^{-3}	1.1967	0.9995	5.15×10^{-3}	1.0893	0.9981	NT

surface coverage [94,98]. Molecular organic coatings can either enhance or inhibit colloid aggregation and retention behaviour. Enhanced colloid interactions have been linked to charge neutralization or bridging of macromolecules [94,96]. Contrarily, inhibited aggregation or retention has been elucidated by an increase in repulsive electrostatic, steric hindrance, or electrosteric interactions [94,99–101]. The case of inhibited aggregation or retention effect can be applied to compare the colloidal suspension systems (SSA850; SSA850 + meth4% + ami4% + star8%; SSA850 + meth5% + ami4% + star8%), where the increase of activation energy is attributed to the increase of apparent viscosity and interfacial tension. This last physical parameter strongly dependent on the interaction energy remains to be confirmed by the use of different methods of measuring surface and interfacial tension. So, in this sense, it can be categorically stated that to envisage situations that are promising or unpromising for colloid aggregation and/or retention mechanism, it is necessary to calculate the interaction energy taking into account the van der Waals and electrostatic double-layer interactions; the particle sizes, shapes and orientation; the curvature and nanoscale surface roughness; and finally the steric or electrosteric

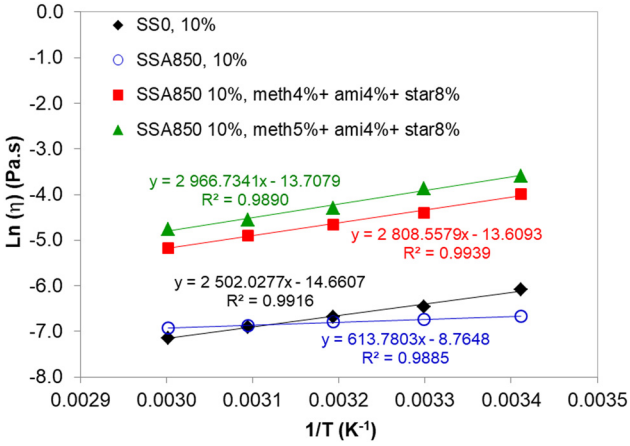

Figure 14: Arrhenius plots of ln(η) versus 1/T for sludge systems (SS0, SSA850, SSA850 mixed with 4% methocel + 4% amijel + 8% starch, and SSA850 mixed with 5% methocel + 4% amijel + 8% starch), at TS = 10%.

barrier energies [94–101]. This last one is considered the vital parameter tuning sludge rheology. Because the electrical characteristics follow the same temperature-dependence relationships as the rheological characteristics with

Table 9: Fitting parameters of different viscosity rheological models for a TS = 10% of SS0, SSA850, SSA850 + 4% methocel + 4% amijel + 8% starch, and SSA850 + 5% methocel + 4% amijel + 8% starch at different testing temperatures (20, 30, 40, 50, and 60°C)

Sludge	T (°C)	Cross model					Carreau model				
		$\eta = \eta_\infty + \frac{(\eta_0 - \eta_\infty)}{1+(\lambda\dot{\gamma})^m}$					$\eta = \eta_\infty + \left[(\eta_0 - \eta_\infty)(1 + (\lambda\dot{\gamma})^2)^{\frac{n-1}{2}}\right]$				
		η_∞ (Pa s)	η_0 (Pa s)	λ (s)	m	R^2	η_∞ (Pa s)	η_0 (Pa s)	λ (s)	n	R^2
SS0	20	2.28×10^{-3}	0.59	13.16	0.95	0.9985	2.336×10^{-3}	0.05	0.71	7.59×10^{-4}	0.9920
	30	1.556×10^{-3}	0.43	5.33	1.03	0.9987	1.510×10^{-3}	0.39	5.68	6.91×10^{-4}	0.9982
	40	1.258×10^{-3}	0.20	3.57	0.97	1.0000	1.353×10^{-3}	0.06	0.95	1.00×10^{-3}	0.9988
	50	1.006×10^{-3}	0.09	1.43	1.03	1.0000	1.010×10^{-3}	0.04	0.73	7.47×10^{-4}	0.9980
	60	1.017×10^{-3}	0.10	1.51	1.07	0.9982	7.905×10^{-4}	0.06	1.07	1.79×10^{-4}	0.9989
SSA850	20	1.267×10^{-3}	0.41	6.20	1.00	0.9990	1.237×10^{-3}	0.06	0.85	7.56×10^{-4}	0.9881
	30	1.175×10^{-3}	0.09	1.38	1.07	0.9994	1.105×10^{-3}	0.05	0.87	7.53×10^{-4}	0.9969
	40	1.126×10^{-3}	0.15	2.01	1.11	1.0000	9.833×10^{-4}	0.23	4.52	6.65×10^{-4}	0.9979
	50	1.030×10^{-3}	0.26	3.78	1.09	1.0000	8.731×10^{-4}	0.46	9.00	4.63×10^{-4}	0.9927
	60	9.888×10^{-4}	0.14	1.87	1.13	0.9987	7.800×10^{-4}	0.31	5.91	1.77×10^{-4}	0.9973
SSA850 + 4% methocel + 4% amijel + 8% starch	20	1.854×10^{-2}	1.66	7.90	0.96	1.0000	1.862×10^{-2}	1.22	5.38	1.53×10^{-4}	0.9993
	30	1.230×10^{-2}	0.25	2.25	0.78	1.0000	1.208×10^{-2}	0.11	1.01	2.80×10^{-1}	0.9997
	40	9.526×10^{-3}	0.16	1.86	0.86	0.9967	9.319×10^{-3}	0.18	3.96	2.47×10^{-1}	0.9961
	50	7.444×10^{-3}	0.08	0.55	1.16	0.9933	7.328×10^{-3}	0.06	0.61	7.49×10^{-4}	0.9923
	60	5.679×10^{-3}	0.05	0.38	1.44	0.9782	5.494×10^{-3}	0.36	6.30	1.74×10^{-4}	0.9592
SSA850 + 5% methocel + 4% amijel + 8% starch	20	2.762×10^{-2}	0.79	28.88	0.62	0.9974	3.043×10^{-2}	0.09	0.29	5.00×10^{-4}	0.9701
	30	2.092×10^{-2}	0.26	2.33	0.75	1.0000	2.019×10^{-2}	0.13	1.19	3.44×10^{-1}	1.0028
	40	1.357×10^{-2}	0.28	7.17	0.67	0.9999	1.334×10^{-2}	0.22	7.68	3.90×10^{-1}	0.9963
	50	1.048×10^{-2}	0.20	3.12	0.83	0.9950	1.043×10^{-2}	0.08	1.04	2.12×10^{-1}	0.9930
	60	8.577×10^{-3}	0.06	0.35	1.37	0.9766	8.378×10^{-3}	0.07	0.82	1.79×10^{-4}	0.9700

Table 10: Initial value of dynamic viscosity (η_0) and activation energy calculated from Arrhenius plots of sludge systems (SS0, SSA850, SSA850 + 4% methocel + 4% amijel + 8% starch, and SSA850 + 5% methocel + 4% amijel + 8% starch) at TS = 10%

Samples	TS (%)	(η_0) (Pa s)	E_a (kJ mol^{-1})	R^2
SS0	10	4.29×10^{-7}	20.80	0.9916
SSA850	10	1.56×10^{-4}	5.10	0.9885
SSA850 + meth4%+ ami4%+ star8%	10	1.23×10^{-6}	23.35	0.9939
SSA850 + meth5%+ ami4%+ star8%	10	1.11×10^{-6}	24.67	0.9890

the same activation energies, the same interactions are most likely involved in both the rheological and electrical properties [85].

4 Conclusion

In this current work, we have investigated the evolution of rheological characteristics of SS0 and SSAs in relation to calcination temperature, organic additives percentages, TS, and testing temperature. In parallel, the impact of calcination temperature on the elemental composition, structural, specific surface area, and microstructural changing of sludge was also investigated.

It was found that for all TS (4–15%), SS0 and SSAs exhibit non-Newtonian shear thickening (yield dilatant) and non-thixotropic behaviours in terms of shear stress and encompass both shear-thinning laminar and shear-thickening turbulent behaviours in terms of apparent viscosity. According to Herschel–Bulkley and Cross models, both the yield stress and the infinite apparent viscosity of all sludges increased by increasing the TS (from 4 to 15%) and decreased by increasing the calcination temperature (from 800 to 950°C). This last decrease of rheological characteristics can be related not only to the sludge chemical composition and crystalline phase variation, but also to the decrease of BET specific surface area from 10.28 to 3.15 m^2/g and the average pore diameter from 26.58 to 9.60 nm when calcination temperature increased from 800 to 950°C.

The incorporation of organic additives (4% methocel, 4% amijel, and 8% starch) in SSA sludges, at high TS (10–15%), has conducted to a shear-thinning (pseudoplastic) behaviour, where yield stress and infinite apparent viscosity are increased. These two characteristics showed a significant rise when the methocel percentage increases from 2 to 6%. In addition, roughly the thixotropic behaviour of SSA mixed with 4% methocel, 4% amijel, and 8% starch was shown enhanced and weakened, respectively, when TS and calcination temperature increased.

As the results of testing temperature rise, a meaningful decrease in shear stress and apparent viscosity of sludge systems was noticed. Hence, the relationship between temperature and apparent viscosity of many sludge systems was characterized by temperature-dependent activation energy. The sludge system composed of SSA850 mixed with 5% methocel, 4% amijel, and 8% starch exhibited the highest inter-particle strength (E_a = 24.67 kJ mol^{-1}) followed by the system consisted of SSA850 mixed with 4% methocel, 4% amijel, and 8% starch (E_a = 23.35 kJ mol^{-1}), then the SS0 system (E_a = 20.80 kJ mol^{-1}), and finally the SSA850 system (E_a = 5.10 kJ mol^{-1}). This explains the negative and positive impact, respectively, of the calcination temperature and the percentage of organic additives on activation energy.

From the perspective of this research, we suggest carrying out an extended analysis on the use of SSA's obtained at different calcination temperatures as efficient adsorbents or as low-cost tubular ceramic membranes for heavy metal ions removal from industrial effluents and is also interesting to study the effect of alkaline or acid pretreatment of SSA's on the removal efficiency of heavy metals from industrial wastewater.

Funding information: This work was supported financially by the Directorate General for Scientific Research and Technological Development (DGRSDT), the Ministry of Higher Education and Scientific Research of Algeria (PRFU project code: B00L01UN350120200004).

Author contributions: Amar Bestani: methodology, formal analysis, investigation, and visualization; Choukri Lekbir: supervision, investigation, methodology, conceptualization, writing – original draft, writing – review & editing. Abdelbaki Benmounah: project administration and resources.

Conflict of interest: The authors state no conflict of interest.

Data availability statement: The datasets generated during and/or analysed during the current study are available from the corresponding author on reasonable request.

Ethical approval: The conducted research is not related to either human or animal use.

References

[1] Vesilind PA. Treatment and disposal of wastewater sludges. 2nd edn. Michigan: Ann Arbor Science; 1979.

[2] Hall JE, ed. Alternative uses for sewage sludge. Proceedings of a conference organised by Wrc Medmenham and held at the university of York. 1989 Sept 5–7. York, UK. Oxford: Pergamon Press; 1991.

[3] Outwater A, Tansel B. Reuse of sludge and minor wastewater residuals. 1st edn. Florida: CRC Press; 1994.

[4] Hing CL, Zenz DR, Tata P, Kuchenrither R, Malina Jr JF, Sawyer B. Municipal sewage sludge management: A reference text on processing, utilization and disposal. 2nd edn. Basel: CRC Press; 1998.

[5] Dhir RK, Limbachiya MC, McCarthy MJ. Recycling and reuse of sewage sludge. Proceedings of the international symposium organised by concrete technology unit and held at the university of Dundee. 2001 March 19–20. Dundee, Scotland, UK. London: Thomas Telford Ltd; 2001.

[6] Twardowska I, Schramm KW, Berg K. Sewage sludge. In: Twardowska I, editor. Solid waste: Assessment, monitoring and remediation. Oxford: Elsevier; 2004. p. 239–95.

[7] Sanin FD, Clarkson WW, Vesilind PA. Sludge engineering: The treatment and disposal of wastewater sludges. 1st edn. Pennsylvania: DEStech Publications; 2011.

[8] Guangyin Z, Youcai Z. Pollution control and resource recovery for sewage sludge. 1st edn. Oxford: Butterworth-Heinemann, Elsevier; 2017.

[9] Prasad MNV, de Campos Favas PJ, Vithanage M, Mohan SV. Industrial and municipal sludge: Emerging concerns and scope for resource recovery. 1st edn. Oxford: Butterworth-Heinemann, Elsevier; 2019.

[10] Zhang S, Wang F, Mei Z, Lv L, Chi Y. Status and development of sludge incineration in China. Waste Biomass Valoriz. 2021;12(7):3541–74. doi: 10.1007/s12649-020-01217-9.

[11] Rajput VD, Yadav AN, Jatav HS, Singh SK, Minkina T. Sustainable management and utilization of sewage sludge. 1st edn. Switzerland: Springer Cham; 2022.

[12] Khan S, Naushad M, Al-Gheethi A, Iqbal J. Engineered nanoparticles for removal of pollutants from wastewater: Current status and future prospects of nanotechnology for remediation strategies. J Environ Chem Eng. 2021;9(5):106160. doi: 10.1016/j.jece.2021.106160.

[13] Hoang SA, Bolan N, Madhubashani AMP, Vithanage M, Perera V, Wijesekara H, et al. Treatment processes to eliminate potential environmental hazards and restore agronomic value of sewage sludge: A review. Environ Pollut. 2022;293:118564. doi: 10.1016/j.envpol.2021.118564.

[14] Hyrycz M, Ochowiak M, Krupińska A, Włodarczak S, Matuszak M. A review of flocculants as an efficient method for increasing the efficiency of municipal sludge dewatering: Mechanisms, performances, influencing factors and perspectives. Sci Total Environ. 2022;820:153328. doi: 10.1016/j.scitotenv.2022.153328.

[15] Zhu Y, Zhai Y, Li S, Liu X, Wang B, Liu X, et al. Thermal treatment of sewage sludge: A comparative review of the conversion principle, recovery methods and bioavailability-predicting of phosphorus. Chemosphere. 2022;291:133053. doi: 10.1016/j.chemosphere.2021.133053.

[16] Weiner RF, Matthews RA. Hazardous waste. In: Weiner RF, Matthews RA, editors. Environmental engineering. Oxford: Butterworth-Heinemann, Elsevier; 2003. 295–311.

[17] Smith SR. A critical review of the bioavailability and impacts of heavy metals in municipal solid waste composts compared to sewage sludge. Environ Int. 2009;35(1):142–56. doi: 10.1016/j.envint.2008.06.009.

[18] Lynn CJ, Dhir RK, Ghataora GS. Environmental impacts of sewage sludge ash in construction: Leaching assessment. Resour Conserv Recycl. 2018;136:306–14. doi: 10.1016/j.resconrec.2018.04.029.

[19] Tarpani RRZ, Alfonsín C, Hospido A, Azapagic A. Life cycle environmental impacts of sewage sludge treatment methods for resource recovery considering ecotoxicity of heavy metals and pharmaceutical and personal care products. J Environ Manage. 2020;260:109643. doi: 10.1016/j.jenvman.2019.109643.

[20] Krishna D, Sachan HK, Jatav HS. Management of sewage sludge for environmental sustainability. In: Rajput VD, Yadav AN, Jatav HS, Singh SK, Minkina T, editors. Sustainable management and utilization of sewage sludge. Switzerland: Springer Cham; 2022. p. 353–81.

[21] Kwapinski W, Kolinovic I, Leahy JJ. Sewage sludge thermal treatment technologies with a focus on phosphorus recovery: a review. Waste Biomass Valoriz. 2021;12(11):5837–52. doi: 10.1007/s12649-020-01280-2.

[22] Kacprzak M, Neczaj E, Fijałkowski K, Grobelak A, Grosser A, Worwag M, et al. Sewage sludge disposal strategies for sustainable development. Environ Res. 2017;156:39–46. doi: 10.1016/j.envres.2017.03.010.

[23] Kominko H, Gorazda K, Wzorek Z. Effect of sewage sludge-based fertilizers on biomass growth and heavy metal accumulation in plants. J Environ Manage. 2022;305:114417. doi: 10.1016/j.jenvman.2021.114417.

[24] Zhang H, Qi HY, Zhang YL, Ran DD, Wu LQ, Wang HF, et al. Effects of sewage sludge pretreatment methods on its use in agricultural applications. J Hazard Mater. 2022;428:128213. doi: 10.1016/j.jhazmat.2022.128213.

[25] Đurđević D, Blecich P, Jurić Ž. Energy recovery from sewage sludge: The case study of Croatia. Energies. 2019;12(10):1–19. doi: 10.3390/en12101927.

[26] Zamparas M. The role of resource recovery technologies in reducing the demand of fossil fuels and conventional fossil-based mineral fertilizers. In: Kyriakopoulos GL, editor. Low carbon energy technologies in sustainable energy systems. Oxford: Academic Press, Elsevier; 2021. p. 3–24.

[27] Istuque DB, Soriano L, Akasaki JL, Melges JLP, Borrachero MV, Monzó J, et al. Effect of sewage sludge ash on mechanical and microstructural properties of geopolymers based on metakaolin. Constr Build Mater. 2019;203:95–103. doi: 10.1016/j.conbuildmat.2019.01.093.

[28] Payá J, Monzó J, Borrachero MV, Soriano L. Sewage sludge ash. In: de Brito J, Agrela F, editors. New trends in eco-efficient and recycled concrete. Cambridge: Woodhead Publishing Elsevier; 2019. p. 121–52.

[29] Zat T, Bandieira M, Sattler N, Segadães AM, Cruz RCD, Mohamad G, et al. Potential re-use of sewage sludge as a raw material in the production of eco-friendly bricks. J Environ Manage. 2021;297:113238. doi: 10.1016/j.jenvman.2021.113238.

[30] Fink J. Cement additives. In: Fink J, editor. Petroleum engineer's guide to oil field chemicals and fluids. Gulf Oxford: Professional Publishing; 2021. p. 441–92.
[31] Kumar M, Shreelaxmi P, Kamath M. Review on characteristics of sewage sludge ash and its partial replacement as binder material in concrete. In: Das BB, Nanukuttan SV, Patnaik AK, Panandikar NS, editors. Recent trends in civil engineering. Singapore: Springer; 2021. p. 65–78.
[32] Rozada F, Calvo LF, García AI, Villacorta JM, Otero M. Dye adsorption by sewage sludge-based activated carbons in batch and fixed-bed systems. Bioresour Technol. 2003;87(3):221–30. doi: 10.1016/S0960-8524(02)00243-2.
[33] Dutta S, Gupta B, Srivastava SK, Gupta AK. Recent advances on the removal of dyes from wastewater using various adsorbents: a critical review. Mater Adv. 2021;2(14):4497–31. doi: 10.1039/D1MA00354B.
[34] Kumar RV, Goswami L, Pakshirajan K, Pugazhenthi G. Dairy wastewater treatment using a novel low cost tubular ceramic membrane and membrane fouling mechanism using pore blocking models. J Water Process Eng. 2016;13:168–75. doi: 10.1016/j.jwpe.2016.08.012.
[35] Mouratib R, Achiou B, El Krati M, Younssi SA, Tahiri S. Low-cost ceramic membrane made from alumina- and silica-rich water treatment sludge and its application to wastewater filtration. J Eur Ceram Soc. 2020;40(15):5942–50. doi: 10.1016/j.jeurceramsoc.2020.07.050.
[36] Behn VC. Experimental determination of sludge flow parameters. J San Eng Div. 1962;88(3):39–54. doi: 10.1061/JSEDAI.0000386.
[37] Campbell HW, Crescuolo PJ. The use of rheology for sludge characterization. Water Sci Technol. 1982;14(6–7):475–89. doi: 10.2166/wst.1982.0120.
[38] Spinosa L. Technological characterization of sewage sludge. Waste Manage Res. 1985;3(4):389–98. doi: 10.1016/0734-242X(85)90132-6.
[39] Lotito V, Spinosa L, Mininni G, Antonacci R. The rheology of sewage sludge at different steps of treatment. Water Sci Technol. 1997;36(11):79–85. doi: 10.1016/S0273-1223(97)00672-0.
[40] Baudez JC, Ayol A, Coussot P. Practical determination of the rheological behavior of pasty biosolids. J Environ Manage. 2004;72(3):181–8. doi: 10.1016/j.jenvman.2004.04.011.
[41] Baudez JC. Physical aging and thixotropy in sludge rheology. Appl Rheol. 2008;18(1):13459–66. doi: 10.1515/arh-2008-0003.
[42] Baudez JC, Slatter P, Eshtiaghi N. The impact of temperature on the rheological behaviour of anaerobic digested sludge. Chem Eng J. 2013;215–216:182–7. doi: 10.1016/j.cej.2012.10.099.
[43] Ratkovich N, Horn W, Helmus FP, Rosenberger S, Naessens W, Nopens I, et al. Activated sludge rheology: A critical review on data collection and modeling. Water Res. 2013;47(2):463–82. doi: 10.1016/j.watres.2012.11.021.
[44] Eshtiaghi N, Markis F, Yap SD, Baudez JC, Slatter P. Rheological characterisation of municipal sludge: A review. Water Res. 2013;47(15):5493–510. doi: 10.1016/j.watres.2013.07.001.
[45] Lotito V, Lotito AM. Rheological measurements on different types of sewage sludge for pumping design. J Environ Manage. 2014;137:89–96. doi: 10.1016/j.jenvman.2014.02.005.
[46] Hong E, Yeneneh AM, Sen TK, Ang HM, Kayaalp A. A comprehensive review on rheological studies of sludge from various sections of municipal wastewater treatment plants for enhancement of process performance. Adv Colloid Interface Sci. 2018;257:19–30. doi: 10.1016/j.cis.2018.06.002.
[47] Canziani R, Spinosa L. Sludge from wastewater treatment plants. In: Prasad MNV, De Campos Favas PJ, Vithanage M, Mohan SV, editors. Industrial and municipal sludge emerging, concerns and scope for resource recovery. Oxford: Butterworth-Heinemann, Elsevier; 2019. p. 3–30.
[48] Spinosa L, Ayol A. Rheological characterization of sludge. In: Prasad MNV, De Campos Favas PJ, Vithanage M, Mohan SV, editors. Industrial and municipal sludge emerging, concerns and scope for resource recovery. 1st edn. Oxford: Butterworth-Heinemann, Elsevier; 2019. p. 225–52.
[49] Miryahyaei S, Olinga K, Ayub MS, Jayaratna SS, Othman M, Eshtiaghi N. Rheological measurements as indicators for hydrolysis rate, organic matter removal, and dewaterability of digestate in anaerobic digesters. J Environ Chem Eng. 2020;8(4):1–12. doi: 10.1016/j.jece.2020.103970.
[50] Wei P, Tan Q, Uijttewaal W, van Lier JB, de Kreuk M. Experimental and mathematical characterisation of the rheological instability of concentrated waste activated sludge subject to anaerobic digestion. Chem Eng J. 2018;349:318–26. doi: 10.1016/j.cej.2018.04.108.
[51] Ionescu CM, Birs IR, Copot D, Muresan CI, Caponetto R. Mathematical modelling with experimental validation of viscoelastic properties in non-Newtonian fluids. Phil Trans R Soc A. 2020;378(2172):1–21. doi: 10.1098/rsta.2019.0284.
[52] Baroutian S, Eshtiaghi N, Gapes DJ. Rheology of a primary and secondary sewage sludge mixture: Dependency on temperature and solid concentration. Bioresour Technol. 2013;140:227–33. doi: 10.1016/j.biortech.2013.04.114.
[53] Zhang J, Haward SJ, Wu Z, Dai X, Tao W, Li Z. Evolution of rheological characteristics of high-solid municipal sludge during anaerobic digestion. Appl Rheol. 2016;26(3):1–10. doi: 10.3933/ApplRheol-26-32973.
[54] Tixier N, Guibaud G, Baudu M. Effect of pH and ionic environment changes on interparticle interactions affecting activated sludge flocs: A rheological approach. Environ Technol. 2003;24(8):971–78. doi: 10.1080/09593330309385635.
[55] Manoliadis O, Bishop PL. Temperature effect on rheology of sludges. J Environ Eng. 1984;110(1):286–90. doi: 10.1061/(ASCE)0733-9372(1984)110:1(286).
[56] Hong E, Yeneneh AM, Kayaalp A, Sen TK, Ang HM, Kayaalp M. Rheological characteristics of municipal thickened excess activated sludge (TEAS): impacts of pH, temperature, solid concentration and polymer dose. Res Chem Intermed. 2016;42(8):6567–85. doi: 10.1007/s11164-016-2482-2.
[57] Gienau T, Kraume M, Rosenberger S. Rheological characterization of anaerobic sludge from agricultural and bio-waste biogas plants. Chem Ing Tech. 2018;90(7):988–97. doi: 10.1002/cite.201700102.
[58] Wei P, Uijttewaal W, van Lier JB, de Kreuk M. Impacts of shearing and temperature on sewage sludge: Rheological characterisation and integration to flow assessment. Sci Total Environ. 2021;774:1–9. doi: 10.1016/j.scitotenv.2021.145005.
[59] Yeneneh AM, Hong E, Sen TK, Kayaalp A, Ang HM. Effects of temperature, polymer dose, and solid concentration on the rheological characteristics and dewaterability of digested sludge of wastewater treatment plant (WWTP). Water Air Soil Pollut. 2016;227(4):1–14. doi: 10.1007/s11270-016-2820-4.
[60] Pollice A, Giordano C, Laera G, Saturno D, Mininni G. Rheology of sludge in a complete retention membrane bioreactor. Environ Technol. 2006;27(7):723–32. doi: 10.1080/09593332708618690.

[61] Han S, Yue Q, Yue M, Gao B, Li Q, Yu H, et al. The characteristics and application of sludge-fly ash ceramic particles (SFCP) as novel filter media. J Hazard Mater. 2009;171(1-3):809–14. doi: 10.1016/j.jhazmat.2009.06.074.

[62] Mukherjee D, Kar S, Mandal A, Ghosh S, Majumdar S. Immobilization of tannery industrial sludge in ceramic membrane preparation and hydrophobic surface modification for application in atrazine remediation from water. J Eur Ceram Soc. 2019;39(10):3235–46. doi: 10.1016/j.jeurceramsoc.2019.04.008.

[63] Abdullayev A, Bekheet MF, Hanaor DAH, Gurlo A. Materials and applications for low-cost ceramic membranes. Membranes. 2019;9(9):1–31. doi: 10.3390/membranes9090105.

[64] Wang Z, Xu Z, Qiu D, Chu Y, Tang Y. Beneficial utilization of Al/Si/O-rich solid wastes for environment-oriented ceramic membranes. J Hazard Mater. 2021;401:1–10. doi: 10.1016/j.jhazmat.2020.123427.

[65] Thommes M, Kaneko K, Neimark AV, Olivier JP, Reinoso FR, Rouquerol J, et al. Physisorption of gases, with special reference to the evaluation of surface area and pore size distribution (IUPAC Technical Report). Pure Appl Chem. 2015;87(9-10):1051–69. doi: 10.1515/pac-2014-1117.

[66] Zhu X, Zhao L, Fu F, Yang Z, Li F, Yuan W, et al. Pyrolysis of predried dewatered sewage sludge under different heating rates: Characteristics and kinetics study. Fuel. 2019;255:1–7. doi: 10.1016/j.fuel.2019.05.174.

[67] Lin X, Mao T, Chen Z, Chen J, Zhang S, Li X, et al. Thermal cotreatment of municipal solid waste incineration fly ash with sewage sludge: Phases transformation, kinetics and fusion characteristics, and heavy metals solidification. J Clean Prod. 2021;317:1–11. doi: 10.1016/j.jclepro.2021.128429.

[68] Karunadasa KSP, Manoratne CH, Pitawala HM, Rajapakse RM. Thermal decomposition of calcium carbonate (calcite polymorph) as examined by in-situ high-temperature X-ray powder diffraction. J Phys Chem Solids. 2019;134:21–8. doi: 10.1016/j.jpcs.2019.05.023.

[69] Kosanović C, Stubičar N, Tomašić N, Bermanec V, Stubičar M. Synthesis of a forsterite powder by combined ball milling and thermal treatment. J Alloy Compd. 2005;389(1–2):306–9. doi: 10.1016/j.jallcom.2004.08.015.

[70] Kang N, Schmidt MW, Poli S, Franzolin E, Connolly JAD. Melting of siderite to 20 GPa and thermodynamic properties of $FeCO_3$-melt. Chem Geol. 2015;400:34–43. doi: 10.1016/j.chemgeo.2015.02.005.

[71] Majewsky M, Bitter H, Eiche E, Horn H. Determination of microplastic polyethylene (PE) and polypropylene (PP) in environmental samples using thermal analysis (TGA-DSC). Sci Total Environ. 2016;568:507–11. doi: 10.1016/j.scitotenv.2016.06.017.

[72] Rosario DS, Porcel JL, Martínez MP, Castelló DL, López AB. Study of microplastics with semicrystalline and amorphous structure identification by TGA and DSC. J Environ Chem Eng. 2022;10(1):106886. doi: 10.1016/j.jece.2021.106886.

[73] Willems M, Pedersen B, Jørgensen SS. Composition and reactivity of ash from sewage sludge. Ambio. 1976;5(1):32–5.

[74] Nowak B, Aschenbrenner P, Winter F. Heavy metal removal from sewage sludge ash and municipal solid waste fly ash – A comparison. Fuel Process Technol. 2013;105:195–201. doi: 10.1016/j.fuproc.2011.06.027.

[75] Wang L, Skjevrak G, Hustad JE, Grønli MG. Sintering characteristics of sewage sludge ashes at elevated temperatures. Fuel Process Technol. 2012;96:88–97. doi: 10.1016/j.fuproc.2011.12.022.

[76] Bardestani R, Patience GS, Kaliaguine S. Experimental methods in chemical engineering: specific surface area and pore size distribution measurements-BET, BJH, and DFT. Can J Chem Eng. 2019;97(11):2781–91. doi: 10.1002/cjce.23632.

[77] Rosales FJG, Hernández FJR, Sevilla A. An apparent viscosity function for shear thickening fluids. J Non-Newtonian Fluid Mech. 2011;166(5–6):321–5. doi: 10.1016/j.jnnfm.2011.01.001.

[78] Edifor SY, Nguyen QD, van Eyk P, Biller P, Lewis DM. Rheological studies of municipal sewage sludge slurries for hydrothermal liquefaction biorefinery applications. Chem Eng Res Des. 2021;166:148–57. doi: 10.1016/j.cherd.2020.12.004.

[79] Chauhan G, Verma A, Das A, Ojha K. Rheological studies and optimization of Herschel-Bulkley flow parameters of viscous karaya polymer suspensions using GA and PSO algorithms. Rheol Acta. 2018;57(3):267–85. doi: 10.1007/s00397-017-1060-x.

[80] Del-Mazo-Barbara L, Ginebra MP. Rheological characterisation of ceramic inks for 3D direct ink writing: A review. J Eur Ceram Soc. 2021;41(16):18–33. doi: 10.1016/j.jeurceramsoc.2021.08.031.

[81] Cheng Y, Li H. Rheological behavior of sewage sludge with high solid content. Water Sci Technol. 2015;71(11):1686–93. doi: 10.2166/wst.2015.152.

[82] Holzgen M, Quirmbach P. Additives for extrusion. In: Händle F, editor. Extrusion in ceramics. Berlin Heidelberg: Springer-Verlag; 2007. p. 211–20.

[83] Ouallal H, Azrour M, Messaoudi M, Moussout H, Messaoudi L, Tijani N. Incorporation effect of olive pomace on the properties of tubular membranes. J Environ Chem Eng. 2020;8(2):2–9. doi: 10.1016/j.jece.2020.103668.

[84] Tlacuatl GZ, González JP, Arellano JJC, Ramírez HB. Rheological characterization and extrusion of suspensions of natural zeolites. Appl Rheol. 2019;20(3):1–10. doi: 10.3933/applrheol-20-34037.

[85] Ségalen C, Dieudé-Fauvel E, Clément J, Baudez JC. Relationship between electrical and rheological properties of sewage sludge – Impact of temperature. Water Res. 2015;73:1–8. doi: 10.1016/j.watres.2015.01.004.

[86] Nie J, Li M, Liu W, Li W, Xing Z. The role of plasticizer in optimizing the rheological behavior of ceramic pastes intended for stereolithography-based additive manufacturing. J Eur Ceram Soc. 2021;41(1):646–54. doi: 10.1016/j.jeurceramsoc.2020.08.013.

[87] Cao X, Tian Y, Jiang K, Qiu F, Fu K. Evaluation of thermal hydrolysis efficiency of sewage sludge via rheological measurement. J Environ Eng. 2020;146(12):1–12. doi: 10.1061/(ASCE)EE.1943-7870.0001816.

[88] Liu GJ, Liu Y, Wang ZY, Lei YH, Chen ZA, Deng LW. The effects of temperature, organic matter and time-dependency on rheological properties of dry anaerobic digested swine manure. J Waste Manag. 2015;38:449–54. doi: 10.1016/j.wasman.2014.12.015.

[89] Trávníček P, Junga P. Thixotropic behaviour of thickened sewage sludge. J Environ Health Sci Eng. 2014;12(1):1–6. doi: 10.1186/2052-336X-12-72.

[90] Lopez J, Moreau A, Gil JA, van der Graaf JHJM, van Lier JB, Ratkovich N. MBR activated sludge viscosity measurement using the Delft filtration characterization method. J Water Process Eng. 2015;5:35–41. doi: 10.1016/j.jwpe.2014.11.006.

[91] Hassanzadeh M, Tayebi L, Dezfouli H. Investigation of factors affecting on viscosity reduction of sludge from Iranian crude oil storage tanks. Pet Sci. 2018;15(1):634–43. doi: 10.1007/s12182-018-0247-9.

[92] Ceacero CJC, Maroto JMM, Martínez MG, Rodríguez MU, López AB, García CM, et al. Effect of the addition of organic wastes (cork

powder, nut shell, coffee grounds and paper sludge) in clays to obtain expanded lightweight aggregates. Bol Soc Esp Ceram Vidr. 2023;62(1):88–105. doi: 10.1016/j.bsecv.2022.02.007.
[93] Liu M, Zhao Y, Yu Z. Effects of sewage sludge ash produced at different calcining temperatures on pore structure and durability of cement mortars. J Mater Cycles Waste Manag. 2021;23(2):755–63. doi: 10.1007/s10163-021-01174-y.
[94] Bradford SA, Sasidharan S, Kim H, Flores AG, Li T, Shen C. Colloid interaction energies for surfaces with steric effects and incompressible and/or compressible roughness. Langmuir. 2021;37(4):1501–10. doi: 10.1021/acs.langmuir.0c03029.
[95] Hotze EM, Phenrat T, Lowry GV. Nanoparticle aggregation: challenges to understanding transport and reactivity in the environment. J Environ Qual. 2010;39(6):1909–24. doi: 10.2134/jeq2009.0462.
[96] Louie SM, Tilton RD, Lowry GV. Critical review: impacts of macromolecular coatings on critical physicochemical processes controlling environmental fate of nanomaterials. Environ Sci Nano. 2016;3(2):283–10. doi: 10.1039/C5EN00104H.
[97] Pal N, Kumar N, Mandal A. Stabilization of dispersed oil droplets in nanoemulsions by synergistic effects of the gemini surfactant, PHPA polymer, and silica nanoparticle. Langmuir. 2019;35(7):2655–67. doi: 10.1021/acs.langmuir.8b03364.
[98] Petosa AR, Jaisi DP, Quevedo IR, Elimelech M, Tufenkji N. Aggregation and deposition of engineered nanomaterials in aquatic environments: Role of physicochemical interactions. Environ Sci Technol. 2010;44(17):6532–49. doi: 10.1021/es100598h.
[99] Christian P, Von der Kammer F, Baalousha M, Hofmann T. Nanoparticles: structure, properties, preparation and behaviour in environmental media. Ecotoxicology. 2008;17(5):326–43. doi: 10.1007/s10646-008-0213-1.
[100] Aiken GR, Hsu-Kim H, Ryan JN. Influence of dissolved organic matter on the environmental fate of metals, nanoparticles, and colloids. Environ Sci Technol. 2011;45(8):3196–201. doi: 10.1021/es103992s.
[101] Ju-Nam Y, Lead JR. Manufactured nanoparticles: an overview of their chemistry, interactions and potential environmental implications. Sci Total Environ. 2008;400(1–3):396–14. doi: 10.1016/j.scitotenv.2008.06.042.